bioRxiv preprint doi: https://doi.org/10.1101/069229; this version posted August 2, 2017. The copyright holder for this preprint (which was not certified by peer review) is the author/funder, who has granted bioRxiv a license to display the preprint in perpetuity. It is made available under aCC-BY-NC-ND 4.0 International license.

FUN-LDA: A LATENT DIRICHLET ALLOCATION MODEL FOR PREDICTING TISSUE-SPECIFIC FUNCTIONAL EFFECTS OF NONCODING VARIATION

DANIEL BACKENROTH[1], ZIHUAI HE[1], KRZYSZTOF KIRYLUK[2], VALENTINA BOEVA[3,4], LYNN PETHUKOVA[5,6], EKTA KHURANA[7], ANGELA CHRISTIANO[6,8], JOSEPH D. BUXBAUM[9,10], IULIANA IONITA-LAZA[1]

[1] Department of Biostatistics, Columbia University, New York, NY 10032

[2] Department of Medicine, Columbia University, New York, NY 10032

[3] INSERM, U900, F-75005, Paris, France

[4] Institut Curie, Mines ParisTech, PSL Research University, F-75005, Paris, France

[5] Department of Epidemiology, Columbia University, New York, NY 10032

[6] Department of Dermatology, Columbia University, New York, NY 10032

[7] Department of Physiology and Biophysics, Weill Medical College, Cornell University, New York, NY 10021

[8] Department of Genetics and Development, Columbia University, New York, NY 10032

[9] Departments of Psychiatry, Neuroscience, and Genetics and Genomic Sciences, Icahn School of Medicine at Mount SInai, New York, NY 10029

[10] Friedman Brain Institute and Mindich Child Health and Development Institute, Icahn School of Medicine at Mount Sinai, New York, NY 10029

Correspondence to Iuliana Ionita-Laza: ii2135@columbia.edu

bioRxiv preprint doi: https://doi.org/10.1101/069229; this version posted August 2, 2017. The copyright holder for this preprint (which was not certified by peer review) is the author/funder, who has granted bioRxiv a license to display the preprint in perpetuity. It is made available under aCC-BY-NC-ND 4.0 International license.

Abstract

We describe here a new method based on a latent Dirichlet allocation model for predicting functional effects of noncoding genetic variants in a cell type and tissue specific way (FUN-LDA) by integrating diverse epigenetic annotations for specific cell types and tissues from large scale epigenomics projects such as ENCODE and Roadmap Epigenomics. Using this unsupervised approach we predict tissue-specific functional effects for every position in the human genome. We demonstrate the usefulness of our predictions using several validation experiments. Using eQTL data from several sources, including the Genotype-Tissue Expression project, the Geuvadis project and TwinsUK cohort, we show that eQTLs in specific tissues tend to be most enriched among the predicted functional variants in relevant tissues in Roadmap. We further show how these integrated functional scores can be used to derive the most likely cell/tissue type causally implicated for a complex trait using summary statistics from genome-wide association studies, and estimate a tissue-based correlation matrix of various complex traits. We find large enrichment of heritability in functional components of relevant tissues for various complex traits, with FUN-LDA yielding the highest enrichment estimates relative to existing methods. Finally, using experimentally validated functional variants from the literature and variants possibly implicated in disease by previous studies, we rigorously compare FUN-LDA to state-of-the-art functional annotation methods such as GenoSkyline, ChromHMM, Segway, and IDEAS, and show that FUN-LDA has better prediction accuracy and higher resolution compared to these methods. In summary, we describe a new approach and perform rigorous comparisons with the most commonly used functional annotation methods, providing a valuable resource for the community interested in the functional annotation of noncoding variants. Scores for each position in the human genome and for each ENCODE/Roadmap tissue are available from http://www.columbia.edu/∼ii2135/funlda.html.

1. Introduction

Understanding the functional consequences of noncoding genetic variation is one of the most important problems in human genetics. Comparative genomics studies suggest that most of the mammalian conserved and recently adapted regions consist of noncoding elements [1, 2, 3]. Furthermore, most of the loci identified in genome-wide association studies fall in noncoding regions and are likely to be involved in gene regulation in a cell type and tissue specific manner [4]. Noncoding

bioRxiv preprint doi: https://doi.org/10.1101/069229; this version posted August 2, 2017. The copyright holder for this preprint (which was not certified by peer review) is the author/funder, who has granted bioRxiv a license to display the preprint in perpetuity. It is made available under aCC-BY-NC-ND 4.0 International license.

variants are also known to play an important role in cancer. Somatic variants in noncoding regions can act as drivers of tumor progression and germline noncoding variants can act as risk alleles [5]. Thus, improved understanding of tissue-specific functional effects of noncoding variants will have implications for multiple diseases and traits.

Prediction of the functional effects of genetic variation is difficult for several reasons. To begin with, there is no single definition of function. As discussed in [6] there are several possible definitions, depending on whether one considers genetic, evolutionary conservation or biochemical perspectives. These different approaches each have limitations and vary substantially with respect to the specific regions of the human genome that they predict to be functional. In particular the genetic approach, based on experimental evaluation of the phenotypic consequence of a sequence alteration (e.g. by measuring the impact of individual alleles on gene expression in a particular context), is low throughput, laborious and may miss elements that lead to phenotypic effects manifest only in rare cells or specific environmental contexts. The evolutionary approach relies on accurate multispecies alignment which makes it challenging to identify certain functional elements, such as distal regulatory elements, although recently several approaches have been developed for primate- or even human-specific elements [7]. An additional limitation of the evolutionary approach is that it is not sensitive to tissue and cell type. Finally, the biochemical approach adopted by projects such as ENCODE [3] and Roadmap Epigenomics [8], although helpful in identifying potentially regulatory elements in specific contexts, does not provide definitive proof of function since the observed biochemical signatures can occur stochastically and in general are not completely correlated with function. Besides the difficulty in precisely defining function, a challenge is that the use of functional genomics features from ENCODE and Roadmap (e.g. ChIP-seq and DNase I hypersensitive sites signals) are mostly useful for predicting the effects of variants in cis-regulatory elements, such as promoters, enhancers, silencers and insulators. Other classes of functional variants, for example those with effects on post-transcriptional regulation by alteration of RNA secondary structure or RNA-protein interactions would be missed by these features.

Recently, several computational approaches have been proposed to predict functional effects of genetic variation in noncoding regions of the genome based on epigenetic and evolutionary conservation features [2, 9, 10, 11]. These predictions are not specific to particular cell types or tissues. Here we are interested in predicting functional effects of genetic variants in specific cell types and

bioRxiv preprint doi: https://doi.org/10.1101/069229; this version posted August 2, 2017. The copyright holder for this preprint (which was not certified by peer review) is the author/funder, who has granted bioRxiv a license to display the preprint in perpetuity. It is made available under aCC-BY-NC-ND 4.0 International license.

tissues. The ENCODE Project and the Roadmap Epigenomics Project have profiled various epigenetic features, including histone modifications and chromatin accessibility, genome-wide in more than a hundred different cell types and tissues. Histone modifications are chemical modifications of the DNA-binding histone proteins that influence transcription as well as other DNA processes. Particular histone modifications have characteristic genomic distributions [12]. For example, trimethylation of histone H3 lysine 4 (H3K4me3) is associated with promoter regions, monomethylation of histone H3 lysine 4 (H3K4me1) is associated with enhancer regions, and acetylation of histone H3 lysine 27 (H3K27ac) and of histone H3 lysine 9 (H3K9ac) are associated with increased activation of enhancer and promoter regions [8]. Repressive marks include H3K27me3 (trimethylation of histone H3 lysine 27) and H3K9me3 (trimethylation of histone H3 lysine 9), both associated with inactive promoters of protein-coding genes; H3K27me3 is found in facultatively repressed genes by Polycomb-group factors, while H3K9me3 is found in heterochromatin regions corresponding to constitutively repressed genes [13]. There are dozens of chromatin marks assayed in large numbers of different cell types and tissues, and studying them individually is inefficient.

Several unsupervised approaches exist for integration of these epigenetic features in specific cell types and tissues. Such integrative approaches reflect the belief that epigenetic features interact with one another to control gene expression. One class of methods attempts to segment the genome into non-overlapping segments, representing major patterns of chromatin marks, and labels these segments using a small set of labels such as active transcription start site, enhancer, strong transcription, weak transcription, quiescent etc. This class includes methods such as ChromHMM [8, 14, 15] and Segway [16], based on Hidden Markov Models (HMMs) and Dynamic Bayesian Networks respectively. ChromHMM is based on complete pooling of data from multiple tissues and fitting a single model to this superdataset, while Segway is based on fitting separate models to data from each tissue (no pooling). Various extensions of these early segmentation approaches have been proposed. Several approaches have focused on better modeling the read count data using Poisson-lognormal and negative multinomial distributions [17, 18], while others have focused on better modeling of the correlations among related cell types and tissues [19, 20, 21]. Yet another approach attempts to improve the HMM parameter estimation procedure in ChromHMM by replacing the EM algorithm with a spectral learning procedure [22]. Another class of methods focuses

bioRxiv preprint doi: https://doi.org/10.1101/069229; this version posted August 2, 2017. The copyright holder for this preprint (which was not certified by peer review) is the author/funder, who has granted bioRxiv a license to display the preprint in perpetuity. It is made available under aCC-BY-NC-ND 4.0 International license.

exclusively on predicting functional effects of variants, rather than segmenting the genome as discussed above. A recent method in this class, GenoSkyline [23], is based on fitting a two-component mixture model of multivariate Bernoulli distributions to epigenetic data for each tissue separately, and then computing a posterior probability for each variant to be in the functional class.

We introduce here a new integrated functional score that combines different epigenetic features in specific cell types and tissues. Our model is based on the latent Dirichlet allocation (LDA) model [24], a generative probabilistic model used often in the topic modeling literature, that allows joint modeling of data from multiple cell types and tissues. The variant scores in each tissue are modeled as a mixture over latent functional classes. In the mixture distribution, we assume that the mixture components are shared across all the tissues, while the mixture proportions for the different functional classes can vary from tissue to tissue (more details on the model and inference algorithm are given in the Methods section). Since our primary goal is to provide a functional score (as opposed to a functional element annotation) we focus on integrating four activating histone modifications (i.e. H3K4me1, H3K4me3, H3K9ac, H3K27ac) and DNase. For the four activating histone modifications data, we compute "valley" scores (Methods), motivated by previous work showing that within regions of high histone acetylation, local minima (or valleys) are strongly associated with transcription factor binding sites [25]. We fit the LDA model with multiple functional classes to these data, and compute for each position its posterior probability to belong to a functional class. We define the functional score at a position as the sum of posterior probabilities for the designated 'active enhancer' and 'active promoter' classes.

The proposed LDA model has several advantages. First, because the model is fit jointly to data from multiple cell types and tissues, cross-tissue comparisons are meaningful. Second, our method makes no distributional assumptions on the data, allowing us to avoid various data transformations employed by other approaches (such as dichotomization, or other transformations needed to make the data conform more closely to various parametric assumptions), and facilitating the integration of data with arbitrary distributions. Third, by using the valley scores we can improve the precision of locating functional variants relative to methods that utilize smoothed data or peak regions. Fourth, even though we only provide functional scores in the tissues and cell types available in Roadmap, it is easy to perform functional prediction in additional cell types and tissues once the model has been fit to the original Roadmap data. Furthermore, while we regard FUN-LDA as

bioRxiv preprint doi: https://doi.org/10.1101/069229; this version posted August 2, 2017. The copyright holder for this preprint (which was not certified by peer review) is the author/funder, who has granted bioRxiv a license to display the preprint in perpetuity. It is made available under aCC-BY-NC-ND 4.0 International license.

primarily an approach to perform cell type and tissue specific functional prediction in the same sense as the GenoSkyline approach, we explicitly define the functional variants as those falling in 'active promoter' or 'active enhancer' elements.

In the next section, we demonstrate the usefulness of our predictions using several validation experiments. In summary, we present the following results: (1) we provide cell type and tissue specific functional predictions for every possible position in the hg19 human genome for 127 cell types and tissues in Roadmap, (2) we provide a global view of the sharing of predicted functional variants across large number of cell types and tissues, and show that predicted functional variants that fall in promoters are more likely to be shared across many tissues compared with those that fall in enhancers, (3) we show that eQTLs identified in specific tissues from several sources tend to be most enriched among the predicted functional variants in a relevant Roadmap tissue, (4) we use these cell type and tissue specific scores in conjunction with summary statistics from 21 genome-wide association studies (GWAS) to identify the most likely causal cell type/tissue causally implicated for a particular trait, and estimate a tissue-based correlation matrix among these complex traits, (5) we use experimentally validated functional variants in the literature to rigorously compare FUN-LDA with state-of-the-art functional annotation methods such as GenoSkyline, ChromHMM, Segway, and IDEAS.

2. Results

2.1. **FUN-LDA model with nine classes.** Here we use data for four activating histone modifications, namely H3K4me1, H3K4me3, H3K9ac, H3K27ac, and DNase for 127 different cell types and tissues represented in the Roadmap datasets (see Supplemental Tables S1 and S2). Not all of the histone marks were profiled for each of the 127 different cell types and tissues. However, using the relationships between different marks within and across tissues, signal tracks have been predicted for each of these marks across all tissues [8, 15]. We make use of these predicted signal tracks to compute integrated functional scores for every possible position in the human genome for 127 cell types and tissues. Specifically, using the perplexity based criterion (see Methods section) and prior knowledge on the relationship of histone modifications and chromatin states, we investigated models with varying number of classes, and have chosen as our final model a model with nine classes (as shown in Supplemental Figure S1 the perplexity measure begins to plateau

bioRxiv preprint doi: https://doi.org/10.1101/069229; this version posted August 2, 2017. The copyright holder for this preprint (which was not certified by peer review) is the author/funder, who has granted bioRxiv a license to display the preprint in perpetuity. It is made available under aCC-BY-NC-ND 4.0 International license.

starting with models with 9 classes). We fit the LDA model with nine classes to the valley scores for the active histone modification data, and original DNase, and compute posterior probabilities at each position for the different functional classes. The active functional classes correspond to active promoters and active enhancers (Supplemental Figure S2). When comparing with genome segmentation approaches such as ChromHMM (25 state model), Segway and IDEAS we also make a similar partition (see Methods section and Supplemental Table S3). For each position, the sum of the posterior probabilities for the classes in the functional group is used to score the position for both our method and ChromHMM. Segway and IDEAS only provide a functional class assignment for each position for each cell type and tissue in Roadmap, and we use these assignments to identify the functional variants. The proportion of positions in the functional group for each method is shown in Supplemental Figure S3. FUN-LDA, ChromHMM and DNase-narrow (DNase narrow peaks) estimate that an average of 2% of the genome is functional in a cell type or tissue in Roadmap, with the remaining methods producing higher estimates for the size of the functional component.

Sharing of predicted functional variants across tissues and cell types. We compute for each variant in the 1000 Genomes project a probability to be in the functional class for each tissue in Roadmap separately. In Figure 1 we provide a global picture of the sharing of predicted functional variants across tissues in Roadmap using the generalized Jaccard similarity index, a measure of overlap between predicted functional variants in two tissues (see Methods section). General tissue groupings are indicated in different colors. As expected, tissues that are functionally related tend to cluster together. There are roughly three major groups: blood cells (indicated in red), including various primary immune cell subtypes, stem cells (indicated in blue) and a third group corresponding to various solid organs (this grouping is also apparent in the multi-dimensional scaling visualization of the correlations between the functional scores in Supplemental Figure S4; see also [8], [14], and Supplemental Figure S5 for related results using single histone marks).

Overall, the median Jaccard index across all pairs of tissues is 0.24. As a comparison, we have also computed the Jaccard overlap indices using predicted functional variants that fall in promoters, and separately in enhancers (Methods section). The median Jaccard index for variants falling in promoters is 0.33, and 0.16 for variants falling in enhancers, concordant with existing literature

bioRxiv preprint doi: https://doi.org/10.1101/069229; this version posted August 2, 2017. The copyright holder for this preprint (which was not certified by peer review) is the author/funder, who has granted bioRxiv a license to display the preprint in perpetuity. It is made available under aCC-BY-NC-ND 4.0 International license.

showing that there tends to be more sharing across tissues for predicted functional variants in promoters vs. those in enhancers [26].

2.2. **Enrichment analyses using eQTLs from the Genotype-Tissue Expression project, Geuvadis and TwinsUK data.**

eQTLs from the Genotype-Tissue Expression project. The Genotype-Tissue Expression (GTEx) project is designed to establish a comprehensive data resource on genetic variation, gene expression and other molecular phenotypes across multiple human tissues [27]. We focus here on the cis-eQTL results from the GTEx V6 release comprising RNA-seq data on $7,051$ samples in 44 tissues, each with at least 70 samples (Supplemental Table S4). We are interested in identifying for each GTEx tissue the Roadmap tissue that is most enriched in eQTLs from that GTEx tissue relative to other Roadmap tissues (see Methods section). We exclude from analysis the sex-specific GTEx tissues, most of which have no relevant counterpart in Roadmap. These include the following tissues: ovary, vagina, uterus, testis, prostate, breast. In Table 1 we show the top Roadmap tissue for each remaining GTEx tissue, along with the p value from the enrichment test. In most cases, eQTLs from a GTEx tissue show the most enrichment in the functional component of a relevant Roadmap tissue. For example, for liver tissue in GTEx, liver is the Roadmap tissue with the highest enrichment, for pancreas tissue in GTEx, the Roadmap tissue with the highest enrichment is pancreas, for skeletal muscle tissue in GTEx, the most enriched Roadmap tissue is skeletal muscle. However, there are also a few cases where the top tissue is not necessarily the most intuitive one, such is the case for lung and several brain tissues. Generally, the tissues with unexpected combinations tend to either have small sample sizes for eQTL discovery in GTEx (such as brain tissues) or inadequate representation in Roadmap (e.g. thyroid, pituitary gland, artery - tibial, artery - coronary, esophagus - gastroesophageal junction etc.). Most of the mismatches have relatively large p values as well ($p > 0.001$).

eQTLs from the Geuvadis and TwinsUK data. We sought to perform similar analyses using eQTLs identified in other studies, in particular in lymphoblastoid cell lines (LCLs) in the Geuvadis project, and four tissues (fat, lymphoblastoid cell lines, skin and whole blood) using individuals from the TwinsUK cohort. We have focused here on the lead eQTLs (those variants most associated with expression levels [28]), and performed similar enrichment analyses as for the eQTLs from GTEx. As shown in Table 1, the most enriched Roadmap tissue corresponds very well to the tissue of

bioRxiv preprint doi: https://doi.org/10.1101/069229; this version posted August 2, 2017. The copyright holder for this preprint (which was not certified by peer review) is the author/funder, who has granted bioRxiv a license to display the preprint in perpetuity. It is made available under aCC-BY-NC-ND 4.0 International license.

origin used in the eQTL discovery, providing an independent validation of the findings using the eQTLs from GTEx.

2.3. **Prediction of causal tissues for 21 complex traits.** As an application of our scores to complex trait genetics, we use the recently developed stratified linkage disequilibrium (LD) score regression framework [29] to identify the most relevant cell types and tissues for 21 complex traits for which moderate to large GWAS studies have been performed (Table 2; [30]-[50]). The stratified LD score regression approach uses information from all single nucleotide polymorphisms (SNPs) and explicitly models LD to estimate the contribution to heritability of different functional classes of variants. We modify this method to weight SNPs by their tissue specific functional score (e.g. FUN-LDA), and in this way we assess the contribution to heritability of predicted functional SNPs in a particular Roadmap cell type or tissue (see Supplemental Material for more details).

In Table 2 we show the top Roadmap cell type/tissue (the one with the smallest p value from testing whether predicted functional variants in a tissue contribute significantly to SNP heritability) for each of the 21 complex traits using FUN-LDA to predict functional variants in specific cell types and tissues. For most disorders, the top tissue has previously been implicated in their pathogenesis. For example, the top tissues for body mass index (BMI) are brain tissues, consistent with recent findings indicating that BMI-associated loci are enriched for expression in the brain and central nervous system [51]. Similarly, brain represents the top tissue for most neuropsychiatric disorders, education levels, and smoking. Blood-derived and immune cells represent the top tissue for virtually all of the autoimmune conditions available for analysis. For example, GWAS findings for ulcerative colitis map specifically to the regulatory elements in Th17 cells, whereas lymphoblastoid cell lines represent the top cell type for rheumatoid arthritis. Another interesting finding involves primary hematopoietic stem cells for Alzheimer's disease, consistent with emerging data on the involvement of bone marrow-derived immune cells in the pathogenesis of neurodegeneration [53].

Results for other methods are shown in Supplemental Tables S5-S7. Estimates of enrichment (defined as the proportion of SNP heritability in the category divided by the proportion of SNPs in that category) for the functional component in the top tissues in Supplemental Tables S5-S7 are shown in Figure 2. On average across traits, the functional component for the top tissue as defined by FUN-LDA shows the highest enrichment relative to other methods, with approximately 2% of the SNPs (functional in the top tissue) explaining an estimated 32% of SNP heritability.

bioRxiv preprint doi: https://doi.org/10.1101/069229; this version posted August 2, 2017. The copyright holder for this preprint (which was not certified by peer review) is the author/funder, who has granted bioRxiv a license to display the preprint in perpetuity. It is made available under aCC-BY-NC-ND 4.0 International license.

FUN-LDA is followed closely by DNase-narrow and ChromHMM. Methods such as DNase-gapped, GenoSkyline and IDEAS show substantially lower enrichments; e.g. for IDEAS, 7.1% SNPs explain an estimated 52% of heritability. In terms of the top tissues identified by each method, it is difficult to make an objective comparison since the underlying tissues and cell types are not known for many complex traits. However looking at the results in Supplemental Tables S5-S7, one can point out several likely mismatches, such as 'Lung' for coronary artery disease identified by both GenoSkyline and DNase-narrow, or 'Dnd41 T-Cell Leukemia Cell Line' and 'Fetal Thymus' identified for epilepsy by DNase and DNase-narrow, respectively. Notably, for Type 2 Diabetes, FUN-LDA, Segway and DNase-gapped were the only methods to point to pancreatic tissue.

In Figure 3 we show the correlation matrix for the 21 traits based on the Z-scores from the LD score regressions (see Methods section for more details on how these pairwise correlations were estimated). This correlation matrix reflects the extent to which traits share the same causal tissues, rather than the genetic correlation [54]. Three large phenotypic clusters are clearly evident. The most tightly correlated cluster contains autoimmune and inflammatory conditions, including Crohn's disease, alopecia areata, rheumatoid arthritis and IgA nephropathy. As expected, these conditions share highest functional scores in blood-derived immune cells. The second most strongly inter-correlated cluster is driven by scores in neuronal tissues, and consists of BMI, age at menarche, educational attainment, schizophrenia, and smoking history, with somewhat weaker correlations with autism, epilepsy and bipolar disorder. Lastly, there is a clear co-clustering of cardio-metabolic traits that map to the tissues of liver, pancreas, and small intestine. Also, as shown, Alzheimer's disease clusters with LDL, HDL and triglycerides, concordant with recent reports on a link between cardio-vascular disease and Alzheimer's disease [55].

2.4. **Validations of our model's predictions, and comparisons with existing methods for functional annotation.** To further assess the accuracy of our predictions and compare with existing approaches we use variants in the literature that have been experimentally shown to have a regulatory function. We focus on several main lists of variants: (a) eight variants implicated in Mendelian and complex diseases, with additional experimental validation of their functional effects [56]-[63], (b) confirmed regulatory variants from a multiplexed reporter assay in lymphoblastoid cell lines [64], (c) regulatory motifs in $2,000$ predicted human enhancers using a massively parallel

bioRxiv preprint doi: https://doi.org/10.1101/069229; this version posted August 2, 2017. The copyright holder for this preprint (which was not certified by peer review) is the author/funder, who has granted bioRxiv a license to display the preprint in perpetuity. It is made available under aCC-BY-NC-ND 4.0 International license.

reporter assay in two human cell lines, liver carcinoma (HepG2) and erythrocytic leukemia (K562) cell lines [65], and (d) validated enhancers in 167 ultra conserved sequence elements [66].

2.4.1. *Noncoding variants implicated in Mendelian and complex traits with experimentally predicted regulatory function.* We selected the following eight SNPs that have been shown experimentally to have a regulatory function in particular tissues: rs6801957 [56], rs12821256 [57], rs12350739 [58], rs12740374 [59], rs356168 [60], rs2473307 [61], rs227727 [62], and rs144361550 [63]. In Figure 4, Supplemental Figures S6-S11 we show the predictions in ~ 2 kb windows centered at these SNPs from the different approaches: FUN-LDA, GenoSkyline, ChromHMM (25 state model), Segway and IDEAS. For each of these SNPs, we select the tissue in Roadmap that we believe is closest to the tissue used in the original functional studies ([56]-[63], Supplemental Table S8). We summarize below the results for two of the SNPs, rs6801957 and rs12821256, that show more tissue specificity relative to the other SNPs in the set (i.e. are predicted to be functional in a small number of Roadmap tissues). For the remaining six SNPs the results are summarized in the Supplemental Material, and Supplemental Figures S6-S11.

rs6801957: In [56], the authors show that this SNP, found associated in GWAS studies with ECG measures, is associated with lower *SCN5A* expression in heart tissue in humans and mice. In Figure 4 we show the predictions for Roadmap tissue E104, Right Atrium.

rs12821256, a SNP associated with blond hair color in Iceland and the Netherlands, is located in an enhancer and influences expression of the *KITLG* gene in cultured human keratinocytes [57]. In Figure 4 we show the predictions for Roadmap tissue E127, NHEK-Epidermal Keratinocyte Primary Cells.

For both SNPs, FUN-LDA assigns a posterior probability of 1 to be functional in the corresponding tissues. Compared with existing methods, the region predicted functional by FUN-LDA tends to be substantially smaller, and therefore FUN-LDA has better ability to predict the causal variant in a region of interest relative to existing approaches.

2.4.2. *Confirmed regulatory variants (emVars) from a multiplexed reporter assay.* In [64], the authors have applied a new version of the massively parallel reporter assay (MPRA) to identify variants with effects on gene expression. In particular, they apply it to $32,373$ variants from $3,642$ cis-expression quantitative trait loci and control regions in lymphoblastoid cell lines (LCLs),

bioRxiv preprint doi: https://doi.org/10.1101/069229; this version posted August 2, 2017. The copyright holder for this preprint (which was not certified by peer review) is the author/funder, who has granted bioRxiv a license to display the preprint in perpetuity. It is made available under aCC-BY-NC-ND 4.0 International license.

and identify 842 variants showing differential expression between alleles, or emVars, expression-modulating variants. We use this set of 842 emVars as positive control variants. Our negative control variants are those variants tested using the MPRA where neither allele showed differential expression relative to the control, applying a threshold of 0.1 for the Bonferroni corrected p value. After removing from the list of positive and negative control variants those variants that we could not map to a genomic location using the Ensembl database (http://grch37.ensembl.org/index.html), there remained 693 positive control variants and 22,384 negative control variants.

We compute AUC values for several methods, including FUN-LDA, GenoSkyline, ChromHMM (25 state model), Segway and IDEAS. For ChromHMM we partition the twenty-five states into two groups, 'functional' and 'non-functional', with the functional group consisting of 'TssA', 'PromU', 'PromD1', 'PromD2', 'EnhA1', 'EnhA2', 'EnhAF'. For each variant, the sum of ChromHMM posterior probabilities for the classes in the functional group above is used to score the variant. For FUN-LDA we similarly group the designated 'active promoters' and 'active enhancers' classes to form the 'functional' class (see Methods section and Supplemental Table S3). Segway and IDEAS only provide a functional class assignment for each position, and we use these assignments to identify the functional variants. Results are shown in Table 3. As shown, FUN-LDA has higher AUC compared to the existing methods, ChromHMM, GenoSkyline, IDEAS and Segway. Compared with DNase, FUN-LDA performs significantly better than the two binarized versions DNase-narrow and DNase-gapped, the two versions normally used in practice, but it does not outperform the original DNase (on the -log10(p value) scale).

2.4.3. *Regulatory motifs in 2,000 predicted human enhancers using a massively parallel reporter assay.* In [65], the authors use a massively parallel reporter assay to measure the transcriptional levels produced by targeted motif disruptions in 2,104 candidate enhancers in two human cell lines, liver carcinoma (HepG2) and erythrocytic leukemia (K562) cell lines, providing one of the largest resource of experimentally validated enhancer manipulations in human cells. We use as positive control variants those variants where the p value comparing expression values for the sequence with the motif compared to sequences with scrambled versions of the motif was less than 0.05. We use as negative control variants those variants where this p value was greater than 0.1. After removing those variants whose genomic coordinates we could not resolve, there remained, for HepG2, 525 positive and 1,451 negative control variants, and for K562, 342 positive and 1,578 negative control

bioRxiv preprint doi: https://doi.org/10.1101/069229; this version posted August 2, 2017. The copyright holder for this preprint (which was not certified by peer review) is the author/funder, who has granted bioRxiv a license to display the preprint in perpetuity. It is made available under aCC-BY-NC-ND 4.0 International license.

variants. For all methods, we calculate the scores for these motifs by averaging across all bases in the motifs. As shown in Table 3, FUN-LDA has better accuracy compared with GenoSkyline, ChromHMM, IDEAS and Segway, and for HepG2 the improvement is substantial.

We have attempted to form the functional group in an objective manner, based on prior knowledge on what functional classes from the different segmentation approaches (ChromHMM, Segway and IDEAS) should be considered active functional elements. We have performed an additional analysis where we have computed the AUC for all combinations of states (with individual AUC ≥ 0.5) for each segmentation method and selected the state combination with highest AUC for the three datasets above. The results from these analyses are shown in Supplemental Table S10. As shown, even with this optimized state combination, the AUCs for the various methods is most of the times less than for our (unbiasedly selected) state combination for FUN-LDA. Furthermore, the state combination with the maximum AUC often contains states like poised/bivalent promoters that would not a priori be considered functional.

2.4.4. *Ultra conserved sequence elements.* In [66], the authors used extreme evolutionary sequence conservation as a filter to identify putative gene regulatory sequences. Using this approach, they identified 167 ultra conserved sequence elements, and then used transgenic mouse enhancer assay that links each of these candidate elements to a mouse promoter fused to a lacZ reporter gene. In total, 75 out of 167 candidate sequences functioned reproducibly as tissue-specific enhancers of gene expression by the read out of lacZ expression at mouse embryonic day 11.5. Out of 75 positive fragments, 50 mapped to a single anatomical structure in the E11.5 embryonic tissue, while the remaining 25 enhancers directed expression to two or more anatomical structures. Here, we compare the functional scores for the variants falling into these 75 positive enhancers with scores of variants in the remaining 92 elements. In Table 4 we show the top Roadmap tissue for each method and the corresponding AUC values. Notably, most methods, including FUN-LDA, select embryonic tissue as the top tissue, consistent with the conducted experiment. Importantly, FUN-LDA outperforms all other methods except for GenoSkyline in predicting functional elements based on these enhancer assays.

2.4.5. *Widths of predicted functional regions for each method.* In Figure 5 we show the distribution of the widths of predicted functional regions including validated functional variants from the three lists above. The width of the functional region around a variant was determined by finding the

bioRxiv preprint doi: https://doi.org/10.1101/069229; this version posted August 2, 2017. The copyright holder for this preprint (which was not certified by peer review) is the author/funder, who has granted bioRxiv a license to display the preprint in perpetuity. It is made available under aCC-BY-NC-ND 4.0 International license.

width of the window around the variant in which the value of the score is greater than 0.5. Widths are truncated at $20,000$ base pairs (so all widths greater than $20,000$ base pairs are represented as $20,000$ base pairs). The FUN-LDA predicted regions are predicted to be substantially narrower compared to the other methods, hence FUN-LDA has the ability to more precisely and more accurately identify the functional variants in a region of interest compared with existing methods.

3. Discussion

We have introduced here a new unsupervised approach FUN-LDA for the functional prediction of genetic variation in specific cell types and tissues using histone modification and DNase data from the ENCODE and Roadmap Epigenomics projects, and have provided comparisons with commonly used functional annotation methods. FUN-LDA is based on a mixture model that focuses on identifying the narrow regions in the genome whose disruption is most likely to interfere with function in a particular cell type or tissue. Such context specific functional prediction of genetic variation is essential for understanding the function of noncoding variation across cell types and tissues, and for the interpretation of genetic variants uncovered in GWAS and sequencing studies. While existing segmentation approaches can be used to derive a numeric functional score as well, we have shown that they tend to be less accurate at predicting functional effects, and tend to predict wider functional regions compared to the proposed approach. Relative to other recently developed functional scores, such as GenoSkyline, FUN-LDA has substantially better prediction accuracy, and furthermore makes explicit which classes are considered functionally active, namely active promoters and active enhancers, providing an attractive tool for functional scoring of variants.

In terms of prediction accuracy, we have shown FUN-LDA to outperform existing methods, sometimes substantially. We have also shown that DNase can have higher predictive power than FUN-LDA with respect to the MPRA experiments. However not being a probabilistic score is a significant deficiency of DNase (e.g. enrichment analyses as shown here for eQTL and LD score regression are more difficult to implement/interpret) and in practice researchers are normally using DNase peaks rather than the raw DNase scores, and our method significantly outperforms DNase peaks on the metrics we considered. We note also that the experimental datasets we use here (from the MPRA experiments, and validated enhancers in ultra conserved regions) do not have gold standard labels (for example, the sensitivity for the MPRA assay in [64] is estimated to be

bioRxiv preprint doi: https://doi.org/10.1101/069229; this version posted August 2, 2017. The copyright holder for this preprint (which was not certified by peer review) is the author/funder, who has granted bioRxiv a license to display the preprint in perpetuity. It is made available under aCC-BY-NC-ND 4.0 International license.

between $9\% - 24\%$), and therefore there is an upper limit to the AUC we can achieve on these datasets even with an optimal method.

These cell type and tissue specific functional scores have numerous applications. We have shown here for the first time in the literature that eQTLs from several large studies such as GTEx, Geuvadis and TwinUK cohort, are most enriched in the functional components from relevant Roadmap tissues. As shown before in [29], and as illustrated here as well, they can be used to infer the most relevant cell types and tissues for a trait of interest, and can help focus the search for causal variants in complex traits by restricting the set of candidate variants to only those that are predicted to be functional in tissues relevant for the trait under consideration. On average across traits, the functional component for the top tissue as defined by FUN-LDA shows the highest enrichment relative to other methods, with approximately 2% of the SNPs (functional in the top tissue) explaining an estimated 30% of SNP heritability. Beyond the applications shown here, such functional predictions have numerous other applications. They can naturally be used in gene discovery studies to potentially improve power in sequence-based association tests such as SKAT and burden [67], and in fine-mapping studies [68, 69]. They can also be used in identifying regulatory regions that are depleted in functional variation in a specific tissue, similar to recent efforts to identify coding regions that are depleted in functional (e.g. missense, nonsense, and splice acceptor/donor variants) variation [7]. Other applications include improving power of trans-eQTL studies, by using the cell type and tissue specific functional predictions as prior information. Similarly, gene-gene and gene-environment interaction studies can benefit from an analysis focused on variants predicted to be functional in a cell type or tissue relevant to the trait under study.

Choosing the number of functional classes in the LDA model is not an easy task, partly because the number of functional classes is not well defined. We have focused here on a model with nine functional classes based on combining an objective measure such as the perplexity of the model and biological knowledge. There is some subjectivity in any method that seeks to partition the genome into functional classes, both in terms of the number of such classes and their interpretation. Further experiments that produce catalogs of specific types of elements with validated tissue-specific functions would aid in determining the number of states that a genomic annotation model should have, and the interpretation of those states, leading to potential improvements in the accuracy

bioRxiv preprint doi: https://doi.org/10.1101/069229; this version posted August 2, 2017. The copyright holder for this preprint (which was not certified by peer review) is the author/funder, who has granted bioRxiv a license to display the preprint in perpetuity. It is made available under aCC-BY-NC-ND 4.0 International license.

of such functional predictors. Such tissue-specific experimental data would also allow the use of supervised methods which could lead to improved tissue-specific functional scores.

Unlike our method, most of the existing segmentation methods smooth the genomic signal spatially. While they thereby use information from neighboring regions in making predictions for a particular variant, they may be less able to predict functionality of narrow regions with different histone modification profiles from neighboring regions. Another difference between our method and methods that use peak calls is that our method may be better able to integrate weak signals present in several histone marks for prediction. Furthermore, the use of the valley score allows our method to predict functional regions that are narrower in size compared to existing methods.

The Roadmap and ENCODE epigenomes mostly represent average epigenomes over distinct cell populations within a tissue, and it is unknown how the individual cell-types contribute to the average epigenomes. Such a bulk characterization undoubtedly conceals the complexity of epigenetic regulation. Investigation of epigenetic regulation at the single-cell level would provide a more detailed and accurate characterization of the function of variants in each cell. Although single-cell epigenomics data are currently scarce, with rapid technological development of single-cell methods such data should become available over the next few years, and the proposed methods can be readily applied in such settings.

We have computed FUN-LDA posterior probabilities for every position in the human genome for 127 tissue and cell types available in Roadmap. These scores are available at our website and can be imported into the UCSC Genome Browser. Note also that it is easy to make predictions in a new tissue once the model has been fit to the tissues in Roadmap. Furthermore, as with some other existing methods [14], it is possible to make predictions in a new tissue even if not all the epigenetic features we included are available, assuming one can impute the missing features by taking advantage of the correlations of epigenetic signals across both marks and samples as in ChromImpute [15].

Acknowledgments We gratefully acknowledge support by National Institutes of Health grants MH106910 (DB, ZH, II-L), AR065963 (LP, AC), DK105124 and the Herbert Irving Scholars Award (KK), MH100233 and the Seaver Foundation (JDB), the ATIP-Avenir program (VB). We thank Bin Xu and Badri Vardarajan for helpful discussions. We thank Andrew Brown for making the data on lead eQTLs in the Geuvadis and TwinsUK cohort available to us.

bioRxiv preprint doi: https://doi.org/10.1101/069229; this version posted August 2, 2017. The copyright holder for this preprint (which was not certified by peer review) is the author/funder, who has granted bioRxiv a license to display the preprint in perpetuity. It is made available under aCC-BY-NC-ND 4.0 International license.

Web-based resources

1000 Genomes: http://www.1000genomes.org/

ChromHMM: http://compbio.mit.edu/ChromHMM/

ENCODE: https://www.encodeproject.org/

FUN-LDA: http://www.columbia.edu/∼ii2135/funlda.html

GenoSkyline-Plus: http://genoSkyline.med.yale.edu/GenoSkyline

GTEx: http://www.gtexportal.org/home/

IDEAS: http://bx.psu.edu/∼yuzhang/Roadmap_ideas/

Reg2Map: https://personal.broadinstitute.org/meuleman/reg2map/HoneyBadger2-intersect_release/

Roadmap Epigenomics: http://www.roadmapepigenomics.org/

Segway: http://noble.gs.washington.edu/proj/encyclopedia/

UCSC genome browser: https://genome.ucsc.edu/

GWAS summary statistics:

Age at menarche: http://www.reprogen.org/Menarche_Nature2014_GWASMetaResults_17122014.zip

Alopecia areata: http://www.broadinstitute.org/∼sripke/share_links/sRSxpynHPaYRJ1SnYXD17eo3qK8IE6_daner_ALO4_1011b_mdsex/

Alzheimer's disease: http://web.pasteur-lille.fr/en/recherche/u744/igap/igap_download.php

Autism: http://www.med.unc.edu/pgc/files/resultfiles/pgcasdeuro.gz

Bipolar Disorder: http://www.med.unc.edu/pgc/files/resultfiles/pgc.bip.2012-04.zip

BMI, Height: http://www.broadinstitute.org/collaboration/giant/index.php/GIANT_consortium_data_files

Coronary Artery Disease: ftp://ftp.sanger.ac.uk/pub/cardiogramplusc4d/cardiogram_gwas_results.zip

Crohn's Disease: ftp://ftp.sanger.ac.uk/pub/consortia/ibdgenetics/cd-meta.txt.gz

Educational Attainment: http://ssgac.org/documents/SSGAC_Rietveld2013.zip

Epilepsy: http://www.epigad.org/gwas_ilae2014/ILAE_All_Epi_11.8.14.txt.gz

Ever Smoked: http://www.med.unc.edu/pgc/files/resultfiles/tag.evrsmk.tbl.gz

Fasting Glucose: ftp://ftp.sanger.ac.uk/pub/magic/MAGIC_Manning_et_al_FastingGlucose_MainEffect.txt.gz

HDL: http://www.broadinstitute.org/mpg/pubs/lipids2010/HDL_ONE_Eur.tbl.sorted.gz

IGAN: dbGaP Study Accession: phs000431.v2.p1

LDL: http://www.broadinstitute.org/mpg/pubs/lipids2010/LDL_ONE_Eur.tbl.sorted.gz

bioRxiv preprint doi: https://doi.org/10.1101/069229; this version posted August 2, 2017. The copyright holder for this preprint (which was not certified by peer review) is the author/funder, who has granted bioRxiv a license to display the preprint in perpetuity. It is made available under aCC-BY-NC-ND 4.0 International license.

Rheumatoid Arthritis: http://plaza.umin.ac.jp/yokada/datasource/files/GWASMetaResults/RA_GWASmeta_European_v2.txt.gz

Schizophrenia: http://www.med.unc.edu/pgc/files/resultfiles/scz2.snp.results.txt.gz

Triglycerides: http://www.broadinstitute.org/mpg/pubs/lipids2010/TG_ONE_Eur.tbl.sorted.gz

Type 2 Diabetes: http://www.diagram-consortium.org/downloads.html

Ulcerative Colitis: ftp://ftp.sanger.ac.uk/pub/consortia/ibdgenetics/ucmeta-sumstats.txt.gz

4. Methods

4.1. **LDA model for functional annotation.** We propose an application of the latent Dirichlet allocation (LDA) model [24], a generative probabilistic model, in the setting of functional genomics annotations with the goal to compute posterior probabilities for variants to belong to different functional classes.

Let us assume that we have a set of m genetic variants in the training set, together with a set of k functional annotations. For each variant i, we have k tissue-specific functional scores: $\mathbf{Z_i} = (Z_{i1}, \ldots, Z_{ik})$. Let $\mathbf{Z} = (\mathbf{Z_1}, \ldots, \mathbf{Z_m})$ be the set of (continuous) functional scores for all the variants. These scores are epigenetic features (histone modifications and DNase) from ENCODE and Roadmap Epigenomics across a varied set of tissues and cell types. Let l be the number of tissues, and m_j be the number of variants with tissue j annotations in the training set ($m = \sum_{j=1}^{l} m_j$). For each variant $i \leq m$ in the training set we denote by t_i the corresponding tissue (i.e. the annotations corresponding to this variant are for tissue t_i). For each tissue, the variants' scores are represented as a mixture over latent functional classes, where each functional class is characterized by a distribution over variant scores. In what follows, for ease of presentation, we assume only two latent functional classes, but the number of classes can be chosen to be greater than two (see next section for a discussion on the choice of the number of functional classes). We let $\mathbf{C} = (C_1, \ldots, C_m)$ denote the set of indicator variables for all the variants, where $C_i = 1$ if variant i belongs to the first functional class and $C_i = 0$ otherwise. We are not able to observe $\mathbf{C}$.

Let $\boldsymbol{\alpha} = (\alpha_0, \alpha_1)$ be the hyperparameter vector with $\alpha_0, \alpha_1 > 0$. We assume the functional annotation data has been generated from the following generative model:

(1) For each tissue j, choose $(1 - \pi_j, \pi_j) \sim \mathrm{Dir}(\alpha_0, \alpha_1)$.

(2) Given π_j, for each variant i with $t_i = j$ choose a class $C_i \sim \mathrm{Bern}(\pi_j)$.

bioRxiv preprint doi: https://doi.org/10.1101/069229; this version posted August 2, 2017. The copyright holder for this preprint (which was not certified by peer review) is the author/funder, who has granted bioRxiv a license to display the preprint in perpetuity. It is made available under aCC-BY-NC-ND 4.0 International license.

(3) Given $C_1, \ldots, C_m$, $\mathbf{Z}_1, \ldots, \mathbf{Z}_m$ are independently generated with each $\mathbf{Z}_i$ being generated from F_1 if $C_i = 1$, and from F_0 otherwise.

Here $\boldsymbol{\pi} = (\pi_1, \ldots, \pi_l)$ and $\boldsymbol{C}$ are latent variables. We want to calculate the posterior probability for each variant i to be in the first functional class:

$$w_i = P(C_i = 1 \mid \boldsymbol{Z}, \boldsymbol{\alpha}),$$

and the densities f_0 and f_1. Also, we want to estimate the hyperparameter $\boldsymbol{\alpha} = (\alpha_0, \alpha_1)$ empirically using $\boldsymbol{Z}$. For a given tissue the conditional density of $(\pi, \boldsymbol{C})$ given $\boldsymbol{Z}$ and $\boldsymbol{\alpha}$ is:

$$p(\pi, \boldsymbol{C}|\boldsymbol{Z}, \boldsymbol{\alpha}) = \frac{p(\pi, \boldsymbol{C}, \boldsymbol{Z}|\boldsymbol{\alpha})}{p(\boldsymbol{Z}|\alpha)}.$$

For the numerator we have:

$$p(\pi, \boldsymbol{C}, \boldsymbol{Z}|\boldsymbol{\alpha}) = p(\pi|\boldsymbol{\alpha}) \prod_{i=1}^{m} p(C_i|\pi) p(\boldsymbol{Z}_i|C_i).$$

This is easy to compute. However the denominator is not. For the denominator we have:

$$p(\boldsymbol{Z}|\boldsymbol{\alpha}) = \int p(\pi|\boldsymbol{\alpha}) \left(\prod_{i=1}^{m} \sum_{C_i} p(C_i|\pi) p(\boldsymbol{Z}_i|C_i) \right) d\pi.$$

There are 2^m terms in the summation so this is difficult to compute for moderately large m. We propose instead to use a variational approach as described in [24]. In the variational inference approach we first introduce a family of distributions $\{q(\cdot, \cdot|\boldsymbol{a}, \boldsymbol{w})\}$ over the latent variables $(\pi, \boldsymbol{C})$ with its own variational parameters $\boldsymbol{a} = (a_0, a_1)$ and $\boldsymbol{w}$ (these are tissue specific parameters).

Then

$$q(\pi, \boldsymbol{C}|\boldsymbol{a}, \boldsymbol{w}) = q(\pi|\boldsymbol{a}) \prod_{i=1}^{m} q(C_i|w_i),$$

where $q(\pi|\boldsymbol{a})$ is the density of $\mathrm{Dir}(\boldsymbol{a})$ and $q(C_i|w_i)$ is the probability mass function of $\mathrm{Bern}(w_i)$ for $i = 1 \ldots m$.

bioRxiv preprint doi: https://doi.org/10.1101/069229; this version posted August 2, 2017. The copyright holder for this preprint (which was not certified by peer review) is the author/funder, who has granted bioRxiv a license to display the preprint in perpetuity. It is made available under aCC-BY-NC-ND 4.0 International license.

Using Jensen's inequality we have:

$$\begin{aligned}
\log p(\boldsymbol{Z}|\boldsymbol{\alpha}) &= \log \int \sum_{\boldsymbol{C}} p(\boldsymbol{\pi}, \boldsymbol{C}, \boldsymbol{Z}|\boldsymbol{\alpha})\, d\boldsymbol{\pi} \\
&= \log \int \sum_{\boldsymbol{C}} \frac{p(\boldsymbol{\pi}, \boldsymbol{C}, \boldsymbol{Z}|\alpha)}{q(\boldsymbol{\pi}, \boldsymbol{C}|\boldsymbol{a}, \boldsymbol{w})} q(\boldsymbol{\pi}, \boldsymbol{C}|\boldsymbol{a}, \boldsymbol{w})\, d\pi \\
&\geq \int \sum_{\boldsymbol{C}} q(\boldsymbol{\pi}, \boldsymbol{C}|\boldsymbol{a}, \boldsymbol{w}) \log p(\boldsymbol{\pi}, \boldsymbol{C}, \boldsymbol{Z}|\boldsymbol{\alpha})\, d\boldsymbol{\pi} - \int \sum_{\boldsymbol{C}} q(\boldsymbol{\pi}, \boldsymbol{C}|\boldsymbol{a}, \boldsymbol{w}) \log q(\boldsymbol{\pi}, \boldsymbol{C}|\boldsymbol{a}, \boldsymbol{w})\, d\pi \\
&= E_q \log p(\boldsymbol{\pi}, \boldsymbol{C}, \boldsymbol{Z}|\alpha) - E_q \log q(\boldsymbol{\pi}, \boldsymbol{C}|\boldsymbol{a}, \boldsymbol{w}) = L(\boldsymbol{a}, \boldsymbol{w}|\boldsymbol{\alpha}).
\end{aligned}$$

Note that $L(\boldsymbol{a}, \boldsymbol{w}|\boldsymbol{\alpha})$ is a lower bound on the log likelihood. So instead of maximizing the log likelihood directly we maximize this lower bound with respect to the variational parameters $\boldsymbol{a}$ and $\boldsymbol{w}$, as well as the hyperparameter $\boldsymbol{\alpha}$. It can be shown that $\log p(\boldsymbol{Z}|\boldsymbol{\alpha}) - L(\boldsymbol{a}, \boldsymbol{w}|\boldsymbol{\alpha})$ is the Kullback-Leibler (KL) divergence between the true posterior $p(\boldsymbol{\pi}, \boldsymbol{C}|\boldsymbol{\alpha}, \boldsymbol{Z})$ and the variational posterior $q(\boldsymbol{\pi}, \boldsymbol{C}|\boldsymbol{a}, \boldsymbol{w})$ with respect to $q(\boldsymbol{\pi}, \boldsymbol{C}|\boldsymbol{a}, \boldsymbol{w})$. Therefore by maximizing $L(\boldsymbol{a}, \boldsymbol{w}|\boldsymbol{\alpha})$ with respect to $\boldsymbol{a}$ and $\boldsymbol{w}$, we minimize the KL divergence between the variational posterior probability and the true posterior probability. Then we can estimate $P(C_i = 1|\boldsymbol{\alpha}, \boldsymbol{Z})$ by w_i for each variant i. Below we describe the variational inference algorithm.

Variational Inference Algorithm. Assume the initial state $\big(w_1, \ldots, w_m, f_0, f_1, \boldsymbol{\alpha}\big)$. The algorithm proceeds as follows:

Step 1. *(Kernel Density Estimation)*

Fit a multivariate kernel density estimate for each annotation and component separately: f_{0s}^{new} and f_{1s}^{new} for each annotation $s = 1, \ldots, k$, weighting variants by component membership probability. Specifically, for any $\mathbf{x} = (x_1, \ldots, x_k) \in \mathbb{R}^k$ and $s = 1, \ldots, k$, we let

$$f_{0s}^{\text{new}}(x_s) = \frac{\sum_{i=1}^m (1 - w_i) \mathrm{K}_{h_s}(x_s - Z_{is})}{\sum_{i=1}^m (1 - w_i)},$$

and

$$f_{1s}^{\text{new}}(x_s) = \frac{\sum_{i=1}^m w_i \mathrm{K}_{h_s}(x_s - Z_{is})}{\sum_{i=1}^m w_i}.$$

The scaled kernel $\mathrm{K}_{h_s}(a) = \frac{1}{h_s} K(\frac{a}{h_s})$, where $K(\cdot)$ is taken to be the probability density function of a standard normal, and the bandwidth parameter h_s is chosen to be

$$h_s = 0.9 \min\{\mathrm{SD}_s, \mathrm{IQR}_s/1.34\} m^{-1/5}$$

bioRxiv preprint doi: https://doi.org/10.1101/069229; this version posted August 2, 2017. The copyright holder for this preprint (which was not certified by peer review) is the author/funder, who has granted bioRxiv a license to display the preprint in perpetuity. It is made available under aCC-BY-NC-ND 4.0 International license.

according to a rule of thumb due to Silverman [70], where SD_s and IQR_s are the standard deviation and interquartile range of annotation s, respectively. Then

$$f_0^{\text{new}}(\boldsymbol{x}) = \prod_{s=1}^{k} f_{0s}^{\text{new}}(x_s), \quad \text{and} \quad f_1^{\text{new}}(\boldsymbol{x}) = \prod_{s=1}^{k} f_{1s}^{\text{new}}(\boldsymbol{x}).$$

Step 2. *(Variational Step)*

For each tissue j, we obtain w_i for all variants i with $t_i = j$ and (a_0^j, a_1^j) by maximizing the lower bound on the marginal likelihood of $\boldsymbol{Z}$, i.e. $L(\boldsymbol{a}, \boldsymbol{w}|\boldsymbol{\alpha})$, with respect to $\boldsymbol{a}$ and $\boldsymbol{w}$. Details are shown in the Supplemental Material.

This results in the following iterative algorithm:

$$w_i = \frac{f_1(\mathrm{Z}_i)\ \exp(\Psi(a_1^j)))}{f_1(\mathrm{Z}_i)\ \exp(\Psi(a_1^j)) + f_0(\mathrm{Z}_i)\ \exp(\Psi(a_0^j))} \quad \text{for variants } i \text{ with } t_i = j,$$

$$a_0^j = \alpha_0 + \sum_{t_i=j}(1 - w_i) \quad \text{and} \quad a_1^j = \alpha_1 + \sum_{t_i=j} w_i.$$

where $\Psi(x) = d \log \Gamma(x)/dx$ and $\Gamma(x)$ is the Gamma function.

Step 3. *(Newton-Raphson algorithm to estimate the hyperparameters $\boldsymbol{\alpha}$)*

Obtain the empirical Bayes estimate of $\boldsymbol{\alpha} = (\alpha_0, \alpha_1)$ by maximizing the bound $L(\boldsymbol{a}, \boldsymbol{w}|\boldsymbol{\alpha})$ by using Newton-Raphson algorithm where $\boldsymbol{a}$ and $\boldsymbol{w}$ are from Step 2. That is, we find optimal $\boldsymbol{\alpha}$ by iterating:

$$\boldsymbol{\alpha}_{n+1} \leftarrow \boldsymbol{\alpha}_n - H^{-1}(\boldsymbol{\alpha}_n)\nabla L(\boldsymbol{a}^{\text{new}}, \boldsymbol{w}^{\text{new}}|\boldsymbol{\alpha}_n),$$

where $H(\boldsymbol{\alpha})$ is the Hessian matrix evaluated at current $\boldsymbol{\alpha}$.

The gradient $\nabla L(\boldsymbol{\alpha})$ has this form:

$$\frac{\partial L(\boldsymbol{\alpha})}{\partial \alpha_r} = l(\Psi(\alpha_0 + \alpha_1) - \Psi(\alpha_r)) + \sum_{j=1}^{l}(\Psi(a_r^j) - \Psi(a_0^j + a_1^j)) \qquad \text{for } r = 0, 1.$$

The Hessian matrix takes the following form:

$$H(\boldsymbol{\alpha}) = \mathrm{Diag}\big(l\Psi'(\alpha_0), l\Psi'(\alpha_1)\big) - l\Psi'(\alpha_0 + \alpha_1)\mathbf{1}\mathbf{1}'.$$

4.2. **LDA implementation.** We have implemented the above algorithm into an R package, FUN-LDA. In our implementation, we assume a symmetric Dirichlet prior, with $\alpha = 1$, corresponding

bioRxiv preprint doi: https://doi.org/10.1101/069229; this version posted August 2, 2017. The copyright holder for this preprint (which was not certified by peer review) is the author/funder, who has granted bioRxiv a license to display the preprint in perpetuity. It is made available under aCC-BY-NC-ND 4.0 International license.

to a uniform distribution. For training purposes, we select 4000 random variants in each of the 127 tissues. The number of outer iterations in the variational inference algorithm is 250 and the number of inner iterations is 200.

FUN-LDA is computed by fitting the LDA model with nine classes to valley scores for the four activating histone modifications (H3K4me1, H3K4me3, H3K9ac, H3K27ac), and original DNase. For the histone modifications and DNase we start with negative log10 of the Poisson P-value of ChIP-seq or DNase counts relative to expected background counts, as output by ChromImpute [15]. The valley scores are computed as in [25]: for every window of 25 bp, we calculate the maximum score for the two regions from -100 to -500 bp and from 100 to 500 bp. If the score at the window of 25 bp is less than 90% of the minimum of those two maxima, we set the value in that window to that minimum. Otherwise, we set the value in that 25 bp window to 0. For each variant, we get a set of nine posterior probabilities for the variant to be in a specific functional class. To get a functional score, we sum the posterior probabilities for the active functional classes, namely 'active promoters' and 'active enhancers' (Supplemental Figure S2 and Table S3).

4.3. **Prediction in a new tissue.** Once the LDA model has been fit to the epigenetic data for cell types and tissues available in Roadmap, making predictions for a new cell type or tissue is easy. Basically, one only needs to run the iterative algorithm in Step 2 of the variational inference algorithm on the epigenetic data for the new tissue.

4.4. **Choice of number of functional classes in the LDA model based on the perplexity measure.** Choosing the number of functional classes in the LDA model is not straightforward. Too few classes can be insufficient and can lower the accuracy of the resulting classifier. Too many classes can lead to an overly complex model and is subject to overfitting.

Heuristic methods exist based on computing the perplexity of a model with a given number of clusters on held out datasets. Perplexity is used in information theory to describe how well a statistical model fits the data. The lower the perplexity, the better the model, and its generalization performance. In our case, if we let $L(\boldsymbol{Z}_{t_i}) = \log(p(\boldsymbol{Z}_{t_i}|\boldsymbol{\alpha}))$ be the log-likelihood for a held out set of variants for each tissue group t_i, the perplexity is defined as

$$\text{perplexity}(\boldsymbol{Z}_{\text{test}}) = \exp\{-\frac{\sum_{i=1}^{T} L(\boldsymbol{Z}_{t_i})}{\sum_{i=1}^{M} m_i}\},$$

bioRxiv preprint doi: https://doi.org/10.1101/069229; this version posted August 2, 2017. The copyright holder for this preprint (which was not certified by peer review) is the author/funder, who has granted bioRxiv a license to display the preprint in perpetuity. It is made available under aCC-BY-NC-ND 4.0 International license.

where T is the total number of tissues and m_i is the number of variants for tissue t_i. Evaluating the perplexity measure directly is computationally intractable (the computation of the likelihood for each tissue involves a summation over K^{m_i} terms with K being the number of classes), and therefore we use the lower bound on the log-likelihood, i.e. $L(\boldsymbol{a}, \boldsymbol{w}|\boldsymbol{\alpha})$ (see Supplemental Material), to derive an upper bound on the perplexity. This upper bound on the perplexity is referred to as the variational Bayesian bound on the perplexity. In the large data limit, the bound on the log perplexity evaluated on the training data converges to the Bayesian information criterion (BIC) for the model [71]. If the training and testing datasets are assumed to come from the same distributions, then the variational Bayesian bound on the log perplexity converges to the BIC.

4.5. **Alternative functional annotation methods used in our comparisons.** We compare our approach with the following state-of-the-art functional annotation methods.

4.5.1. *Individual histone modifications and DNase scores.* Instead of integrating the various epigenetic marks, one can use the individual scores to predict functional variants. For the histone modifications and DNase we use negative log10 of the Poisson P-value of ChIP-seq or DNase counts relative to expected background counts, as output by ChromImpute [15]. In addition for DNase, we also use narrow peaks and gapped peaks (defined as broad peaks that contain at least one strong narrow peak).

4.5.2. *GenoSkyline - Multivariate Bernoulli mixture models.* A simpler mixture model than the LDA described here is a two-component mixture model $\psi = (\pi, f_0, f_1)$, where f_0 and f_1 are the probability densities for each of the components and π is a mixing parameter. We can fit such a model to data from each tissue separately, and calculate posterior probabilities for each variant to be in the 'functional' class given the observed scores $\mathbf{Z}$, i.e. $P_\psi(C_i = 1|\mathbf{Z})$. For tractability, it is often assumed that the individual scores are conditionally independent given the functional class. Such a two-component multivariate Bernoulli mixture model using dichotomized data from peak calling algorithms has been proposed in [23], an approach called GenoSkyline.

4.5.3. *ChromHMM.* ChromHMM [14] is a method for chromatin state discovery and characterization by integrating multiple chromatin datasets. The underling algorithm is a multivariate Hidden Mixture Model that produces a segmentation of the genome; each segment is assigned a putative function based on enrichment analyses of different biological states in these segments. The

bioRxiv preprint doi: https://doi.org/10.1101/069229; this version posted August 2, 2017. The copyright holder for this preprint (which was not certified by peer review) is the author/funder, who has granted bioRxiv a license to display the preprint in perpetuity. It is made available under aCC-BY-NC-ND 4.0 International license.

ChromHMM 25-state model [15] is based on 12 marks, and, like ours, uses imputed data: H3K4me1, H3K4me2, H3K4me3, H3K9ac, H3K27ac, H4K20me1, H3K79me2, H3K36me3, H3K9me3, H3K27me3, H2A.Z and DNase. ChromHMM is based on complete pooling of data from multiple tissues and fitting a single model to this superdataset.

4.5.4. *Segway.* Segway [16] is a genome segmentation approach, like ChromHMM, based on a dynamic Bayesian network (DBN) model. Segway is based on fitting separate models to data from each tissue. Segmentations for most of the cell types and tissues in Roadmap have been recently generated [72].

4.5.5. *IDEAS.* IDEAS [20] is an integrative and discriminative epigenome annotation algorithm, that like ChromHMM and Segway, segments the genome and assigns each segment a specific functional class. Unlike ChromHMM and Segway, IDEAS models the correlations both along the genome and across cell types. Segmentations for all 127 cell types and tissues in Roadmap have been produced using IDEAS [21].

4.6. **Generalized Jaccard index of overlap.** We are interested in computing a similarity measure of predicted functional variants in two different tissues. Because the distribution of posterior probabilities in any one tissue is highly bimodal, with most of the mass at 0, and a small proportion of variants with posterior probabilities close to 1, in other words we are dealing with sparse binary data, a natural measure of similarity is the Jaccard measure of overlap, defined as follows. If $\mathbf{X} = (x_1, \ldots, x_k)$ and $\mathbf{Y} = (y_1, \ldots, y_k)$ are two vectors with $x_i, y_i \geq 0$ (e.g. vectors of posterior probabilities for variants to be in the functional components for two different tissues), then the generalized Jaccard index of overlap is defined as:

$$J(\mathbf{X}, \mathbf{Y}) = \frac{\sum_i \min(x_i, y_i)}{\sum_i \max(x_i, y_i)}.$$

When $\mathbf{X}$ and $\mathbf{Y}$ are binary vectors, then the Jaccard index of overlap is simply the size of the intersection divided by the size of the union of the two sets. The closer it is to 1, the more overlap there is between the two sets. A Jaccard index of 0 means no overlap.

4.7. **Promoter and tissue-specific enhancer regions.** The promoter region of a protein-coding gene is defined as the union of the regions 2,500 bases upstream of any protein-coding transcripts

bioRxiv preprint doi: https://doi.org/10.1101/069229; this version posted August 2, 2017. The copyright holder for this preprint (which was not certified by peer review) is the author/funder, who has granted bioRxiv a license to display the preprint in perpetuity. It is made available under aCC-BY-NC-ND 4.0 International license.

for the gene, as defined by GENCODE version 24. For enhancer regions we use the Roadmap Stringent enhancer list available at the Reg2Map website.

4.8. **eQTL enrichment.** Let $G_1, \ldots, G_{44}$ be the 44 GTEx tissues with at least 70 samples (Supplemental Table S4), and $R_1, \ldots, R_{127}$ be the 127 Roadmap tissues. For a given tissue in GTEx G_i we are interested in identifying the Roadmap tissue R_j with the highest enrichment in eQTLs from G_i relative to other tissues in Roadmap.

Let

$$p_{G_i|R_j} = \frac{\#\text{eQTLs in tissue } G_i \text{ in functional component } R_j}{\#\text{eQTLs in functional component } R_j}.$$

Note that the number of eQTLs in GTEx tissue G_i is a weighted count, with an eQTL weighted by the inverse of the number of GTEx tissues in which the variant is eQTL, such that $\sum_i p_{G_i|R_j} = 1$. This way eQTLs that are unique to tissue G_i are given higher weight relative to eQTLs that are shared across many tissues. For GTEx tissue G_i, to test whether there is an enrichment in the functional component of Roadmap tissue R_j, we compare $p_{G_i|R_j}$ with

$$p_{G_i|R_{-j}} = \frac{\#\text{eQTLs in tissue } G_i \text{ in functional components excluding } R_j}{\#\text{eQTLs in functional components excluding } R_j}.$$

The null hypothesis is $H_0 : P_{G_i|R_j} = P_{G_i|R_{-j}}$ vs. $H_0 : P_{G_i|R_j} > P_{G_i|R_{-j}}$. We apply a two-sample proportion test for each Roadmap tissue R_j and report the Roadmap tissue with minimum p value in Table 1.

The eQTLs that we used in these analyses are all significantly associated SNP-gene pairs in each of these 44 GTEx tissues, obtained using a permutation threshold-based approach as described by the GTEx Consortium [27]. For the follow-up study making use of eQTLs from Geuvadis and TwinsUK cohort, we use the lead eQTLs, i.e. those eQTLs most strongly associated with gene expression (publicly available for download from [28]).

4.9. **Assessing pairwise correlations among 21 complex traits.** Our aim here is to calculate a correlation matrix of 21 phenotypes based on the Z-scores from the LD score regression procedure, and a p value corresponding to each pair of phenotypes. From the LD score regression approach we obtain a matrix of Z-scores corresponding to 127 ($p = 127$) tissues and 21 ($q = 21$) phenotypes. The main issue we need to take into account when we compute the correlations and the p values is that the tissues are correlated.

bioRxiv preprint doi: https://doi.org/10.1101/069229; this version posted August 2, 2017. The copyright holder for this preprint (which was not certified by peer review) is the author/funder, who has granted bioRxiv a license to display the preprint in perpetuity. It is made available under aCC-BY-NC-ND 4.0 International license.

Let Z_{ij} be the Z-score corresponding to the i-th tissue and j-th phenotype; $\mathbf{Z_i} = (Z_{i1}, \ldots, Z_{iq})$ and $\mathbf{Z^j} = (Z_{1j}, \ldots, Z_{pj})$ be the row/column vectors of matrix $\mathbf{Z}$. Since the elements of $\mathbf{Z}$ are Z-scores, we assume $\mathbf{Z_i} \sim \mathbf{N}(\mathbf{0}, \mathbf{\Sigma_q})$ and $\mathbf{Z^j} \sim \mathbf{N}(\mathbf{0}, \mathbf{\Sigma_p})$.

4.9.1. *Estimation of the correlation matrix.* We aim to estimate $\mathbf{\Sigma_q}$ but the problem is that $\mathbf{Z_i}$'s are not independent. To solve the problem, we propose the following perturbation method.

Let B be the number of perturbation replicates. For the b-th replicate, we generate p independent random variables from $N(0,1)$, $\alpha_{b1}, \ldots, \alpha_{bp}$. Let

$$\mathbf{X_b} = \frac{1}{\sqrt{p}} \sum_{1 \le i \le p} \alpha_{bi} \mathbf{Z_i}.$$

It can be shown that $cov(\mathbf{X_b}) = \mathbf{\Sigma_q}$ and $cov(\mathbf{X_b}, \mathbf{X_{b'}}) = 0$ for any $1 \le b, b' \le B$. So we are able to use the uncorrelated perturbation samples $\mathbf{X_1}, \ldots, \mathbf{X_B}$ to approximate $\mathbf{\Sigma_q}$ and the corresponding correlation matrix $\mathbf{P_q}$. We take $B = 100,000$.

4.9.2. *P values corresponding to all pairs of phenotypes.* For pairs from an uncorrelated bivariate normal distribution, the sampling distribution of a certain function of Pearson's correlation coefficient follows Student's t-distribution with degrees of freedom $M-2$, where M is the number of uncorrelated random variables. Specifically, if the underlying variables have a bivariate normal distribution, the variable

$$t = \rho \sqrt{\frac{M-2}{1-\rho^2}}$$

follows a Student's t-distribution with degrees of freedom $M-2$.

In our case, the number of uncorrelated random variables M depends on the correlation structure of the 127 tissues. M can be understood as the "effective number of tissues". Similar to the calculation of "number of effective tests" by [73], we estimate M by applying an eigen-decomposition to the Jaccard matrix. Suppose $\lambda_1 \ge \lambda_2 \ge \cdots \ge \lambda_p$ are the eigenvalues arranged in descending order. We estimate M by the smallest value such that $\frac{\sum_{i=1}^{M} \lambda_i}{\sum_{i=1}^{p} \lambda_i} > C$. It should be noted that a smaller C will result in more conservative p values as the number of "effective tissues" is smaller, e.g. $M = 124$ when $C = 99.5\%$, $M = 96$ when $C = 95\%$. Too large or too small threshold C may cause M to be either overly liberal or overly conservative. The p values were calculated based on $C = 99.5\%$.

bioRxiv preprint doi: https://doi.org/10.1101/069229; this version posted August 2, 2017. The copyright holder for this preprint (which was not certified by peer review) is the author/funder, who has granted bioRxiv a license to display the preprint in perpetuity. It is made available under aCC-BY-NC-ND 4.0 International license.

4.10. **Code availability.** We have implemented the LDA algorithm into an R package, FUNLDA. The package is available at the Comprehensive R Archive Network (CRAN): https://cran.r-project.org/web/packages/FUNLDA.

References

[1] Lindblad-Toh K et al. (2011) A high-resolution map of human evolutionary constraint using 29 mammals. *Nature* 478: 476–482.

[2] Khurana E et al. (2013) Integrative annotation of variants from 1092 humans: application to cancer genomics. *Science* 342: 1235587.

[3] ENCODE Project Consortium (2012) An integrated encyclopedia of DNA elements in the human genome. *Nature* 489: 57–74.

[4] Altshuler D, Daly MJ, Lander ES (2008) Genetic mapping in human disease. *Science* 322: 881–888.

[5] Khurana E, Fu Y, Chakravarty D, Demichelis F, Rubin MA, Gerstein M (2016) Role of non-coding sequence variants in cancer. *Nat Rev Genet* 17: 93–108.

[6] Kellis M et al. (2014) Defining functional DNA elements in the human genome. *Proc Natl Acad Sci USA* 111: 6131–6138.

[7] Petrovski S, Wang Q, Heinzen EL, Allen AS, Goldstein DB (2013) Genic intolerance to functional variation and the interpretation of personal genomes. *PLoS Genet* 9: e1003709.

[8] Roadmap Epigenomics Consortium (2015) Integrative analysis of 111 reference human epigenomes. *Nature* 518: 317–330.

[9] Kircher M, Witten DM, Jain P, O'Roak BJ, Cooper GM, Shendure J (2014) A general framework for estimating the relative pathogenicity of human genetic variants. *Nat Genet* 46: 310–315.

[10] Fu Y, Liu Z, Lu S, Bedford J, Mu X, Yip K, Khurana E, Gerstein M (2014) FunSeq2: A framework for prioritizing noncoding regulatory variants in cancer. *Genome Biology* 15: 480

[11] Ionita-Laza I, McCallum K, Xu B, Buxbaum JD (2016) A spectral approach integrating functional genomic annotations for coding and noncoding variants. *Nat Genet* 48: 214–220.

[12] Bannister AJ, Kouzarides T (2011) Regulation of chromatin by histone modifications. *Cell Res.* 21(3): 381–395.

[13] Friedman N, Rando OJ (2015) Epigenomics and the structure of the living genome *Genome Res* 25: 1482–1490.

[14] Ernst J, Kellis M (2012) ChromHMM: automating chromatin-state discovery and characterization. *Nature Methods* 9: 215–216.

[15] Ernst J, Kellis M (2015) Large-scale imputation of epigenomic datasets for systematic annotation of diverse human tissues. *Nat Biotechnol* 33: 364–376.

[16] Hoffman MM, Buske OJ, Wang J, Weng Z, Bilmes J, Noble WS (2012) Unsupervised pattern discovery in human chromatin structure through genomic segmentation. *Nat Methods* 9: 473–476.

bioRxiv preprint doi: https://doi.org/10.1101/069229; this version posted August 2, 2017. The copyright holder for this preprint (which was not certified by peer review) is the author/funder, who has granted bioRxiv a license to display the preprint in perpetuity. It is made available under aCC-BY-NC-ND 4.0 International license.

[17] Zacher B, Michel M, Schwalb B, Cramer P, Tresch A, Gagneur J (2017) Accurate Promoter and Enhancer Identification in 127 ENCODE and Roadmap Epigenomics Cell Types and Tissues by GenoSTAN. *PLoS One* 12: e0169249.

[18] Mammana A, Chung HR (2015) Chromatin segmentation based on a probabilistic model for read counts explains a large portion of the epigenome. *Genome Biol* 16: 151.

[19] Biesinger J, Wang Y, Xie X (2013) Discovering and mapping chromatin states using a tree hidden Markov model. *BMC Bioinformatics* Suppl 5: S4.

[20] Zhang Y, An L, Yue F, Hardison RC (2016) Jointly characterizing epigenetic dynamics across multiple human cell types. *Nucleic Acids Res* 44: 6721–6731.

[21] Zhang Y, Hardison RC (2017) Accurate and Reproducible Functional Maps in 127 Human Cell Types via 2D Genome Segmentation. BioRxiv preprint doi: http://dx.doi.org/10.1101/118752.

[22] Song J, Chen KC (2015) Spectacle: fast chromatin state annotation using spectral learning. *Genome Biol* 16: 33.

[23] Lu Q, Powles RL, Wang Q, He BJ, Zhao H (2016) Integrative Tissue-Specific Functional Annotations in the Human Genome Provide Novel Insights on Many Complex Traits and Improve Signal Prioritization in Genome Wide Association Studies. *PLoS Genet* 12: e1005947.

[24] Blei DM, Ng AY, Jordan MI (2003) Latent Dirichlet Allocation. *Journal of Machine Learning Research* 3: 993–1022.

[25] Ramsey S et al. (2010) Genome-wide histone acetylation data improve prediction of mammalian transcription factor binding sites. *Bioinformatics* 26: 2071–2075.

[26] Heintzman ND et al. (2009) Histone modifications at human enhancers reflect global cell-type-specific gene expression. *Nature* 459: 108–112.

[27] The GTEx Consortium (2015) Science. 348: 648–660.

[28] Brown AA, Vi?nuela A, Delaneau O, Spector T, Small K, Dermitzakis ET (2016) Predicting causal variants affecting expression using whole-genome sequence and RNA-seq from multiple human tissues. http://www.biorxiv.org/content/biorxiv/early/2016/11/21/088872.full.pdf

[29] Finucane HK et al. (2015) Partitioning heritability by functional annotation using genome-wide association summary statistics. *Nat Genet* 47: 1228–1235.

[30] Perry JR et al. (2014) Parent-of-origin-specific allelic associations among 106 genomic loci for age at menarche. *Nature* 514: 92–97.

[31] Betz RC et al. (2015) Genome-wide meta-analysis in alopecia areata resolves HLA associations and reveals two new susceptibility loci. *Nat Commun* 6: 5966.

[32] Lambert JC et al. (2013) Meta-analysis of 74,046 individuals identifies 11 new susceptibility loci for Alzheimer's disease. *Nat Genet* 45: 1452–1458.

[33] Cross-Disorder Group of the Psychiatric Genomics Consortium (2013) Identification of risk loci with shared effects on five major psychiatric disorders: a genome-wide analysis. *Lancet* 381: 1371–1379.

bioRxiv preprint doi: https://doi.org/10.1101/069229; this version posted August 2, 2017. The copyright holder for this preprint (which was not certified by peer review) is the author/funder, who has granted bioRxiv a license to display the preprint in perpetuity. It is made available under aCC-BY-NC-ND 4.0 International license.

[34] Psychiatric GWAS Consortium Bipolar Disorder Working Group (2011) Large-scale genome-wide association analysis of bipolar disorder identifies a new susceptibility locus near ODZ4. *Nat Genet* 43: 977–983.

[35] Speliotes EK et al. (2010) Association analyses of 249,796 individuals reveal 18 new loci associated with body mass index. *Nat Genet* 42: 937–948.

[36] Schunkert H et al. (2011) Large-scale association analysis identifies 13 new susceptibility loci for coronary artery disease. *Nat Genet* 43: 333–338.

[37] Jostins L et al. (2012) Host-microbe interactions have shaped the genetic architecture of inflammatory bowel disease. *Nature* 491: 119–124.

[38] Petukhova L, Christiano AM (2016) Functional Interpretation of Genome-Wide Association Study Evidence in Alopecia Areata. *The Journal of investigative dermatology* 136: 314–317.

[39] Xing L et al. (2014) Alopecia areata is driven by cytotoxic T lymphocytes and is reversed by JAK inhibition. *Nature medicine* 20: 1043–1049.

[40] Yokoyama JS et al. (2016) Association Between Genetic Traits for Immune-Mediated Diseases and Alzheimer Disease. *JAMA Neurol* 73: 691-697.

[41] Rietveld CA et al. (2013) GWAS of 126,559 individuals identifies genetic variants associated with educational attainment. *Science* 314: 1467–1471.

[42] International League Against Epilepsy Consortium on Complex Epilepsies (2014) Genetic determinants of common epilepsies: a meta-analysis of genome-wide association studies. *Lancet Neurol* 13: 893–903.

[43] Tobacco and Genetics Consortium (2010) Genome-wide meta-analyses identify multiple loci associated with smoking behavior. *Nat Genet* 42:441–447.

[44] Manning AK et al. (2012) A genome-wide approach accounting for body mass index identifies genetic variants influencing fasting glycemic traits and insulin resistance. *Nat Genet* 44: 659–669.

[45] Teslovich TM et al. (2010) Biological, clinical and population relevance of 95 loci for blood lipids. *Nature* 466: 707–713.

[46] Kiryluk K et al. (2014) Discovery of new risk loci for IgA nephropathy implicates genes involved in immunity against intestinal pathogens. *Nat Genet* 46: 1187–1196.

[47] Okada Y et al. (2014) Genetics of rheumatoid arthritis contributes to biology and drug discovery. *Nature* 506: 376–381.

[48] Schizophrenia Working Group of the Psychiatric Genomics Consortium (2014) Biological insights from 108 schizophrenia-associated genetic loci. *Nature* 511: 421–427.

[49] Morris AP et al. (2012) Large-scale association analysis provides insights into the genetic architecture and pathophysiology of type 2 diabetes. *Nat Genet* 44: 981–990.

[50] Lango AH et al. (2010) Hundreds of variants clustered in genomic loci and biological pathways affect human height. *Nature* 467: 832–838.

[51] Locke AE et al. (2015) Genetic studies of body mass index yield new insights for obesity biology. *Nature* 518: 197–206.

bioRxiv preprint doi: https://doi.org/10.1101/069229; this version posted August 2, 2017. The copyright holder for this preprint (which was not certified by peer review) is the author/funder, who has granted bioRxiv a license to display the preprint in perpetuity. It is made available under aCC-BY-NC-ND 4.0 International license.

[52] Magga J et al. (2012) Production of monocytic cells from bone marrow stem cells: therapeutic usage in Alzheimer's disease. *J Cell Mol Med* 16: 1060–1073.

[53] Gjoneska E, Pfenning AR, Mathys H, Quon G, Kundaje A, Tsai LH, Kellis M (2015) Conserved epigenomic signals in mice and humans reveal immune basis of Alzheimer's disease. *Nature* 518: 365–369.

[54] Bulik-Sullivan B et al. An atlas of genetic correlations across human diseases and traits. *Nat Genet* 47: 1236–1241.

[55] Jefferson AL et al. (2015) Low cardiac index is associated with incident dementia and Alzheimer disease: the Framingham Heart Study. *Circulation* 131: 1333–1339.

[56] van den Boogaard M et al. (2014) A common genetic variant within scn10a modulates cardiac scn5a expression. *J Clin Invest* 124: 1844–1852.

[57] Guenther CA, Tasic B, Luo L, Bedell MA, Kingsley DM (2014) A molecular basis for classic blond hair color in europeans. *Nat Genet* 46: 748–752.

[58] Visser M, Palstra RJ, Kayser M (2014) Human skin color is influenced by an intergenic dna polymorphism regulating transcription of the nearby bnc2 pigmentation gene. *Hum Mol Genet* 23: 5750–5562.

[59] Musunuru K et al. (2010) From noncoding variant to phenotype via SORT1 at the 1p13 cholesterol locus. *Nature* 466: 714–719.

[60] Soldner F et al. (2016) Parkinson-associated risk variant in distal enhancer of ?-synuclein modulates target gene expression. *Nature* 533: 95–99.

[61] Gilks WP, Hill M, Gill M, Donohoe G, Corvin AP, Morris DW (2012) Functional investigation of a schizophrenia gwas signal at the cdc42 gene. *World J Biol Psychiatry* 13: 550–554.

[62] Leslie EJ et al. (2015) Identification of functional variants for cleft lip with or without cleft palate in or near PAX7, FGFR2, and NOG by targeted sequencing of GWAS loci. *Am J Hum Genet* 96: 397–411.

[63] Choi J et al. (2017) A common intronic variant of PARP1 confers melanoma risk and mediates melanocyte growth via regulation of MITF. *Nat Genet* Epub ahead of print

[64] Tewhey R et al. (2016) Direct identification of hundreds of expression-modulating variants using a multiplexed reporter assay. *Cell* 165: 1519–1529.

[65] Kheradpour P, Ernst J, Melnikov A, Rogov P, Wang L, Zhang X, Alston J, Mikkelsen TS, Kellis M (2013) Systematic dissection of regulatory motifs in 2000 predicted human enhancers using a massively parallel reporter assay. *Genome Res* 23: 800–811.

[66] Pennacchio LA et al. (2006) In vivo enhancer analysis of human conserved non-coding sequences. *Nature* 444: 499–502.

[67] Lee S, Wu MC, Lin X (2012) Optimal tests for rare variant effects in sequencing association studies. *Biostatistics* 13: 762–775.

[68] Ionita-Laza I, Capanu M, De Rubeis S, McCallum K, Buxbaum JD (2014) Identification of rare causal variants in sequence-based studies: methods and applications to VPS13B, a gene involved in Cohen syndrome and autism. *PLoS Genet* 10: e1004729.

bioRxiv preprint doi: https://doi.org/10.1101/069229; this version posted August 2, 2017. The copyright holder for this preprint (which was not certified by peer review) is the author/funder, who has granted bioRxiv a license to display the preprint in perpetuity. It is made available under aCC-BY-NC-ND 4.0 International license.

[69] Kichaev G, Yang WY, Lindstrom S, Hormozdiari F, Eskin E, Price AL, Kraft P, Pasaniuc B (2014) Integrating functional data to prioritize causal variants in statistical fine-mapping studies. *PLoS Genet* 10: e1004722.

[70] Silverman BW (1986) Density Estimation for Statistics and Data Analysis, Chapman & Hall, London

[71] Hagai Attias (1999) Inferring parameters and structure of latent variable models by variational bayes. *Proceedings of the Fifteenth conference on Uncertainty in artificial intelligence*, Morgan Kaufmann Publishers Inc., pp. 21-30.

[72] Libbrecht MW, Rodriguez O, Weng Z, Hoffman M, Bilmes JA, Noble WS (2017) A unified encyclopedia of human functional DNA elements through fully automated annotation of 164 human cell types. doi: https://doi.org/10.1101/086025

[73] Xiaoyi G, Starmer J, Martin ER (2008) A multiple testing correction method for genetic association studies using correlated single nucleotide polymorphisms. *Genetic Epidemiology* 32: 361–369.

Table 1. Enrichment of eQTLs from different sources (GTEx, Geuvadis and TwinsUK cohort) among FUN-LDA predicted functional variants in tissues and cell types in Roadmap Epigenomics. The top Roadmap tissue is given for each eQTL tissue, along with the p value from a two-sample proportion test.

Study	Tissue	Roadmap Epigenome Name	-log10(p)
GTEx	Whole Blood	Primary neutrophils from peripheral blood	189.72
	Cells - Transformed fibroblasts	Muscle Satellite Cultured Cells	62.69
	Cells - EBV-transformed lymphocytes	GM12878 Lymphoblastoid Cells	37.74
	Liver	Liver	31.82
	Muscle - Skeletal	Skeletal Muscle Male	19.42
	Heart - Left Ventricle	Fetal Heart	15.83
	Esophagus - Mucosa	Esophagus	12.78
	Pancreas	Pancreas	10.84
	Colon - Transverse	Rectal Mucosa Donor 31	10.46
	Artery - Tibial	Stomach Smooth Muscle	7.74
	Esophagus Muscularis	Stomach Smooth Muscle	6.74
	Thyroid	Fetal Intestine Small	5.96
	Skin - Sun Exposed (Lower leg)	Foreskin Keratinocyte Primary Cells skin03	5.47
	Spleen	Primary B cells from peripheral blood	5.35
	Artery - Aorta	Aorta	5.28
	Brain - Hippocampus	Brain Cingulate Gyrus	5.10
	Small Intestine - Terminal Ileum	Fetal Intestine Large	5.04
	Heart - Atrial Appendage	Fetal Heart	4.90
	Adipose - Subcutaneous	Adipose Nuclei	4.74
	Colon - Sigmoid	Colon Smooth Muscle	4.62
	Brain - Caudate (basal ganglia)	Brain Substantia Nigra	4.17
	Brain - Cerebellum	Adipose Derived Mesenchymal Stem Cell Cultured Cells	4.12
	Nerve - Tibial	Brain Hippocampus Middle	4.11
	Adrenal Gland	Fetal Adrenal Gland	3.94
	Skin - Not Sun Exposed (Suprapubic)	Foreskin Keratinocyte Primary Cells skin03	3.56
	Brain - Putamen (basal ganglia)	Brain Substantia Nigra	3.36
	Brain - Cerebellar Hemisphere	Brain Angular Gyrus	3.08
	Stomach	Stomach Mucosa	3.02
	Lung	Osteoblast Primary Cells	2.57
	Brain - Cortex	Mesenchymal Stem Cell Derived Chondrocyte Cultured Cells	2.10
	Adipose - Visceral (Omentum)	Primary T helper cells from peripheral blood	2.00
	Pituitary	Primary T helper cells PMA-I stimulated	1.96
	Brain - Nucleus accumbens (basal ganglia)	H9 Cells	1.80
	Esophagus - Gastroesophageal Junction	Primary neutrophils from peripheral blood	1.64
	Brain - Frontal Cortex (BA9)	NHDF-Ad Adult Dermal Fibroblast Primary Cells	1.61
	Artery - Coronary	Primary B cells from peripheral blood	1.35
	Brain - Hypothalamus	Osteoblast Primary Cells	1.29
	Brain - Anterior cingulate cortex (BA24)	A549 EtOH 0.02pct Lung Carcinoma Cell Line	1.04
Geuvadis	Lymphoblastoid cell line	GM12878 Lymphoblastoid Cells	8.57
TwinsUK	Blood	Primary neutrophils from peripheral blood	7.54
	Fat	Mesenchymal Stem Cell Derived Adipocyte Cultured Cells	6.80
	Skin	Foreskin Keratinocyte Primary Cells skin02	3.62
	Lymphoblastoid cell line	GM12878 Lymphoblastoid Cells	3.08

bioRxiv preprint doi: https://doi.org/10.1101/069229; this version posted August 2, 2017. The copyright holder for this preprint (which was not certified by peer review) is the author/funder, who has granted bioRxiv a license to display the preprint in perpetuity. It is made available under aCC-BY-NC-ND 4.0 International license.

Table 2. Top cell type/tissue in Roadmap for 21 GWAS traits using FUN-LDA posterior probabilities. The p value from the stratified LD score regression, as well as the GWAS sample size are reported for each trait.

Trait	Roadmap Epigenome Name	-log10(p)	n_{GWAS}
Schizophrenia	Fetal Brain Female	14.69	82,315
Height	Mesenchymal Stem Cell Derived Chondrocyte Cultured Cells	12.27	133,653
Rheumatoid Arthritis	GM12878 Lymphoblastoid Cells	6.92	58,284
Crohn's Disease	Primary B cells from cord blood	6.24	20,883
Age at Menarche	H9 Derived Neuronal Progenitor Cultured Cells	6.14	132,989
Educational Attainment	Fetal Brain Female	5.83	101,069
BMI	Brain Germinal Matrix	4.79	123,865
HDL	Liver	4.72	99,900
Coronary Artery Disease	Liver	4.60	86,995
Ulcerative Colitis	Primary T helper 17 cells PMA-I stimulated	4.44	27,432
Type2 Diabetes	Pancreatic Islets	4.20	69,033
Epilepsy	Brain Anterior Caudate	4.11	34,853
Triglycerides	Liver	4.10	96,598
LDL	Liver	4.08	95,454
Alopecia Areata	Primary T cells from cord blood	3.90	7,776
Alzheimer's	Primary hematopoietic stem cells G-CSF-mobilized Male	3.78	54,162
IGAN	Primary Natural Killer cells from peripheral blood	3.28	11,946
Bipolar Disorder	Fetal Brain Female	3.19	16,731
Ever Smoked	Brain Inferior Temporal Lobe	2.67	74,035
Autism	Primary monocytes from peripheral blood	2.40	10,263
Fasting Glucose	Pancreatic Islets	1.44	58,074

bioRxiv preprint doi: https://doi.org/10.1101/069229; this version posted August 2, 2017. The copyright holder for this preprint (which was not certified by peer review) is the author/funder, who has granted bioRxiv a license to display the preprint in perpetuity. It is made available under aCC-BY-NC-ND 4.0 International license.

bioRxiv preprint doi: https://doi.org/10.1101/069229; this version posted August 2, 2017. The copyright holder for this preprint (which was not certified by peer review) is the author/funder, who has granted bioRxiv a license to display the preprint in perpetuity. It is made available under aCC-BY-NC-ND 4.0 International license.

TABLE 3. AUC values for discriminating between variants likely to be functional and control variants. Results are shown for several datasets (three tissues) with experimental validation (MPRA) of potential regulatory variants. Methods include FUN-LDA, GenoSkyline, ChromHMM (25 state model), Segway, IDEAS, and DNase (original, -narrow and -gapped).

Dataset	Method	AUC
emVars in [64], E116	FUN-LDA	0.709
	GenoSkyline	0.662
	ChromHMM	0.668
	Segway	0.624
	IDEAS	0.621
	DNase	0.716
	DNase-narrow	0.629
	DNase-gapped	0.653
Regulatory motifs in [65], E118/HepG2	FUN-LDA	0.694
	GenoSkyline	0.629
	ChromHMM	0.608
	Segway	0.618
	IDEAS	0.546
	DNase	0.719
	DNase-narrow	0.561
	DNase-gapped	0.550
Regulatory motifs in [65], E123/K562	FUN-LDA	0.646
	GenoSkyline	0.620
	ChromHMM	0.634
	Segway	0.585
	IDEAS	0.615
	DNase	0.654
	DNase-narrow	0.524
	DNase-gapped	0.565

bioRxiv preprint doi: https://doi.org/10.1101/069229; this version posted August 2, 2017. The copyright holder for this preprint (which was not certified by peer review) is the author/funder, who has granted bioRxiv a license to display the preprint in perpetuity. It is made available under aCC-BY-NC-ND 4.0 International license.

TABLE 4. AUC values for discriminating between variants likely to be functional and control variants. Results are shown for validated enhancers in ultra conserved sequence elements [66]. Methods include FUN-LDA, GenoSkyline, ChromHMM (25 state model), Segway, IDEAS, and DNase (original, -narrow and -gapped). The tissue with the highest AUC for each method is also shown.

Dataset	Method	Top Tissue	AUC
Ultraconserved Elements	FUN-LDA	hESC Derived CD184+ Endoderm Cultured Cells	0.658
	GenoSkyline	Primary hematopoietic stem cells	0.697
	ChromHMM	hESC Derived CD56+ Ectoderm Cultured Cells	0.604
	Segway	HUES6 Cells	0.588
	IDEAS	hESC Derived CD184+ Endoderm Cultured Cells	0.646
	DNase	hESC Derived CD184+ Endoderm Cultured Cells	0.629
	DNase-narrow	hESC Derived CD184+ Endoderm Cultured Cells	0.568
	DNase-gapped	hESC Derived CD184+ Endoderm Cultured Cells	0.656

bioRxiv preprint doi: https://doi.org/10.1101/069229; this version posted August 2, 2017. The copyright holder for this preprint (which was not certified by peer review) is the author/funder, who has granted bioRxiv a license to display the preprint in perpetuity. It is made available under aCC-BY-NC-ND 4.0 International license.

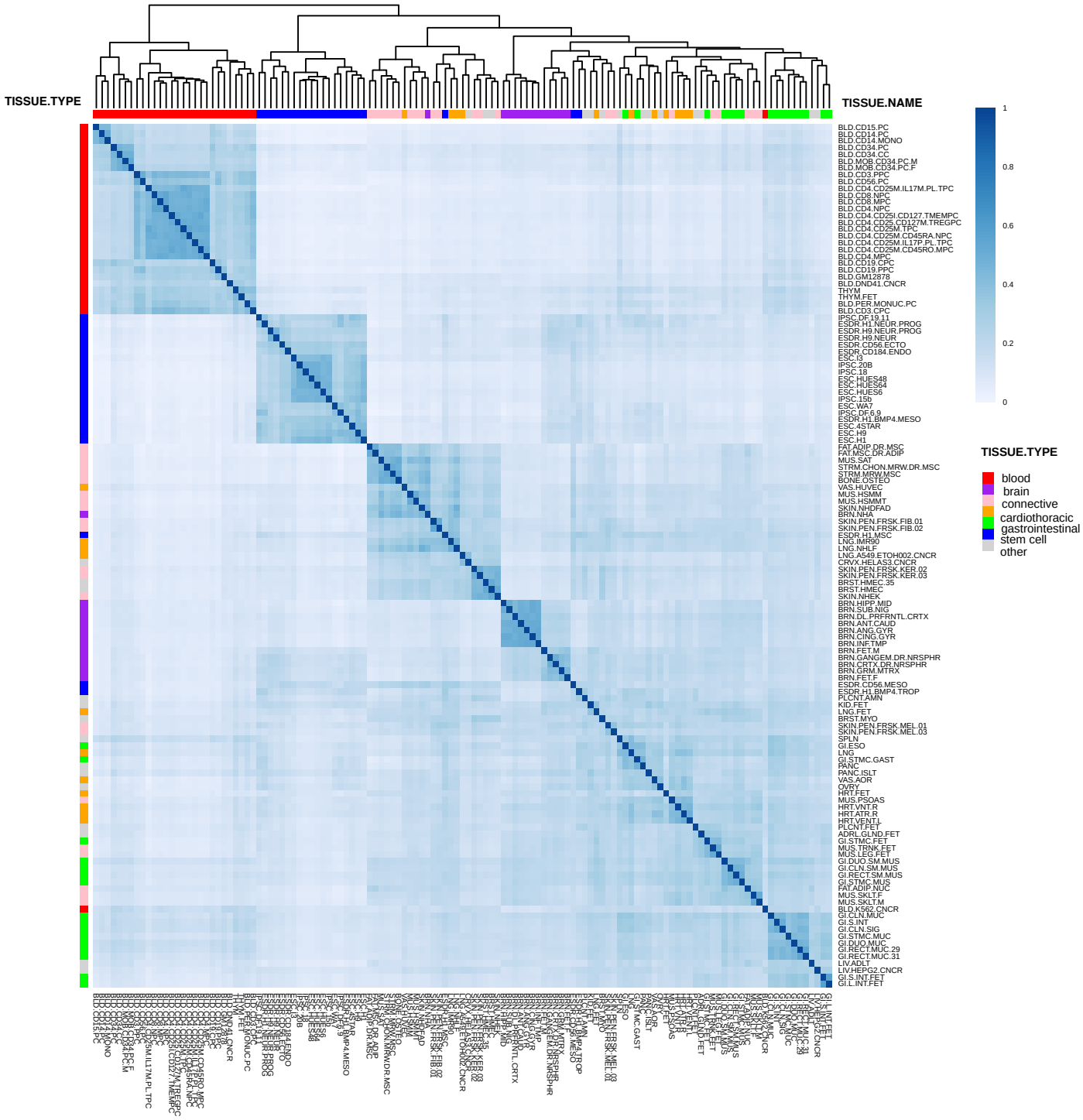

FIGURE 1. Jaccard index of overlap among functional variants in different cell types and tissues in Roadmap Epigenomics. Hierarchical clustering is used to cluster the different cell types and tissues.

bioRxiv preprint doi: https://doi.org/10.1101/069229; this version posted August 2, 2017. The copyright holder for this preprint (which was not certified by peer review) is the author/funder, who has granted bioRxiv a license to display the preprint in perpetuity. It is made available under aCC-BY-NC-ND 4.0 International license.

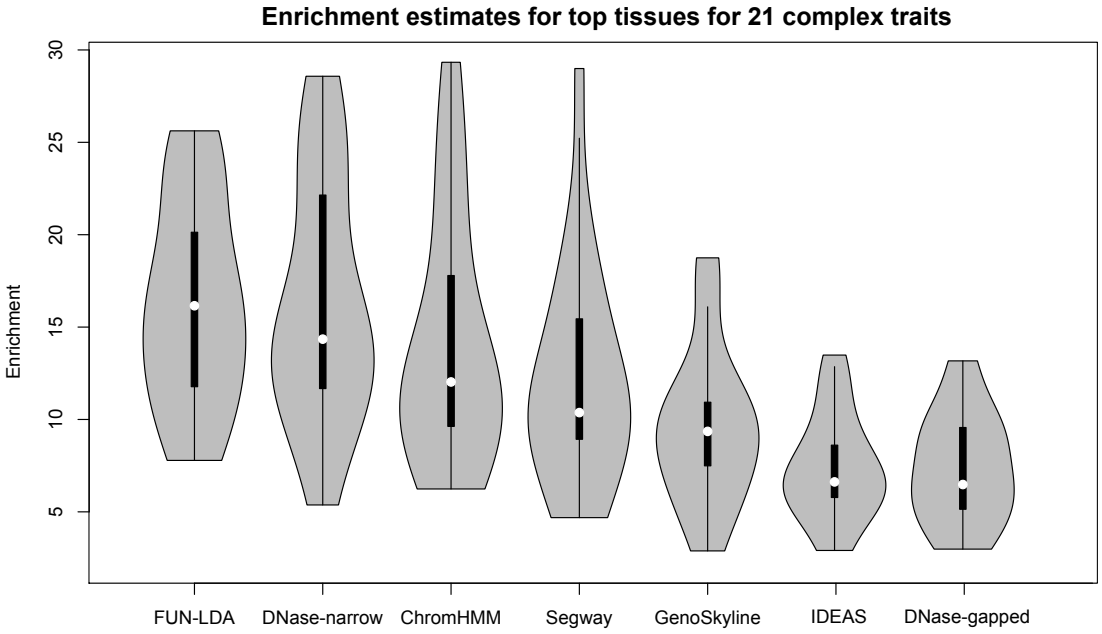

FIGURE 2. Enrichment estimates (the proportion of SNP heritability in the functional component divided by the proportion of SNPs in that component) for different methods across top tissues for 21 complex traits. Enrichment estimates for DNase are omitted since they do not make sense for continuous annotations, such as DNase.

bioRxiv preprint doi: https://doi.org/10.1101/069229; this version posted August 2, 2017. The copyright holder for this preprint (which was not certified by peer review) is the author/funder, who has granted bioRxiv a license to display the preprint in perpetuity. It is made available under aCC-BY-NC-ND 4.0 International license.

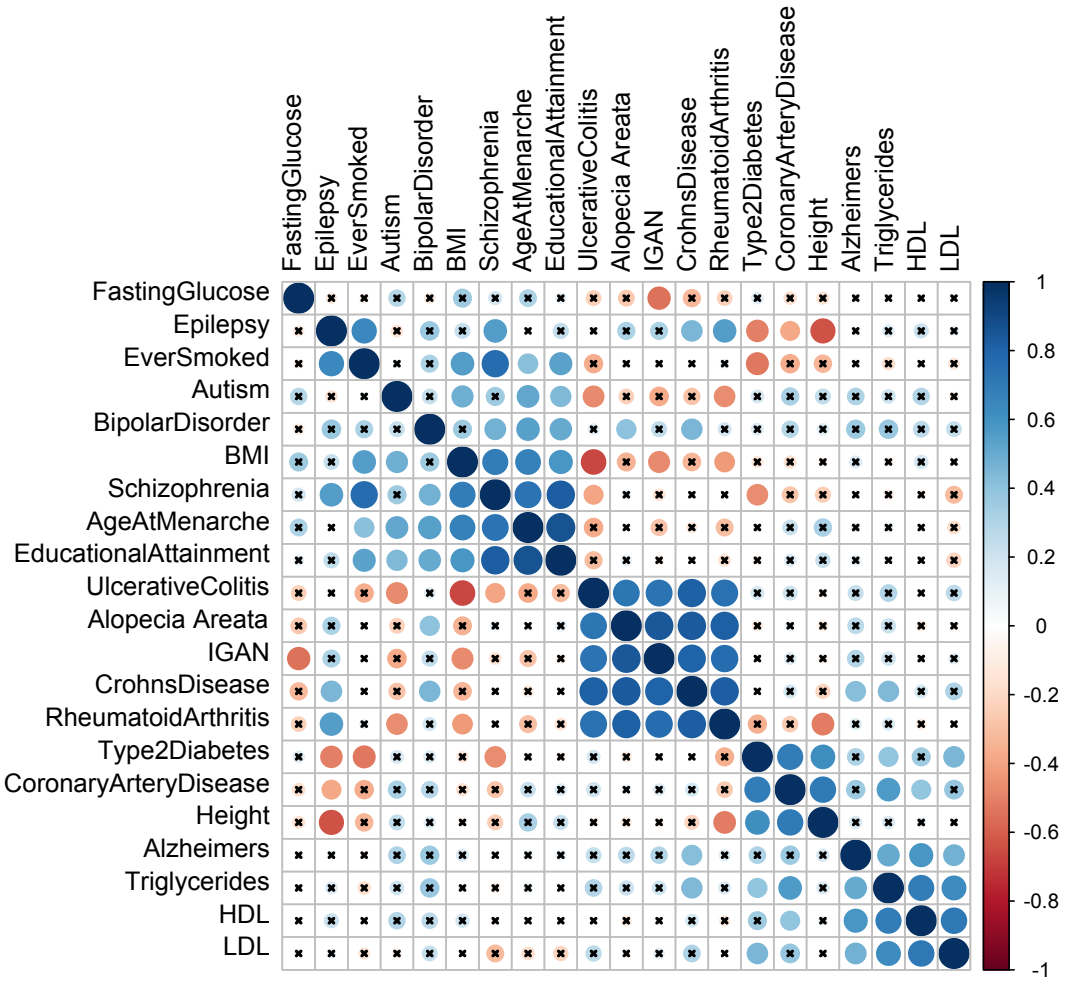

FIGURE 3. Tissue Correlations for 21 common traits. Hierarchical clustering (average linkage method) is used to cluster diseases. The '**x**' symbol indicates that those correlations are not significant at the 0.0001 level.

bioRxiv preprint doi: https://doi.org/10.1101/069229; this version posted August 2, 2017. The copyright holder for this preprint (which was not certified by peer review) is the author/funder, who has granted bioRxiv a license to display the preprint in perpetuity. It is made available under aCC-BY-NC-ND 4.0 International license.

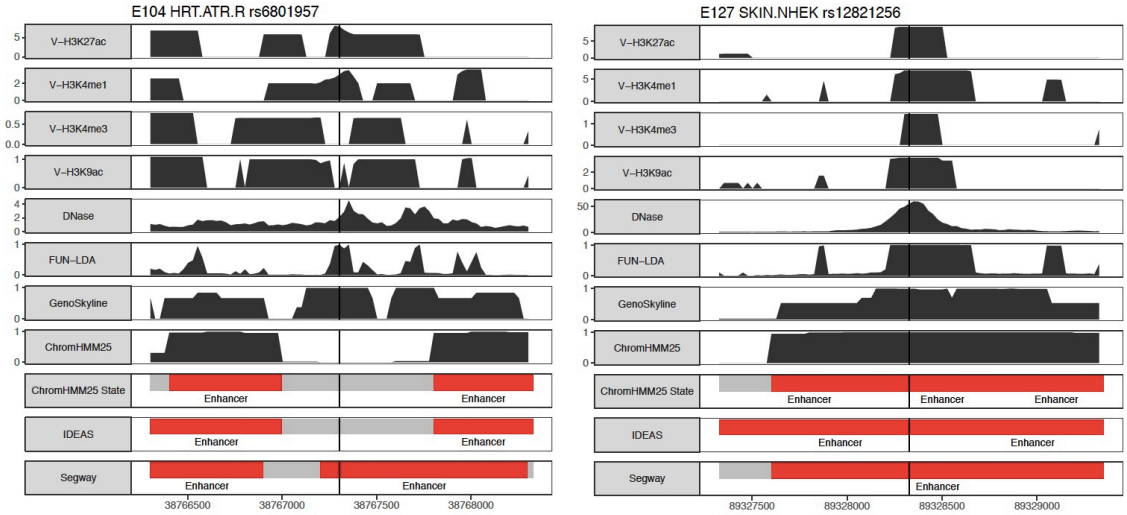

(A) rs6801957 in Roadmap tissue E104. (B) rs12821256 in Roadmap tissue E127.

FIGURE 4. Valley scores for four activating histone marks and DNase, posterior probabilities from FUN-LDA, GenoSkyline, and ChromHMM (25 state model), and segmentations from ChromHMM, IDEAS and Segway are shown in 2 kb windows centered around the lead SNPs. For clarity we only highlight in the segmentations the type of states we consider functional (enhancer states in red, promoter states in blue) for the different segmentation approaches.

SUPPLEMENTAL MATERIAL

Stratified LD score regression approach to identify the tissue of interest. The stratified LD score regression approach [1] uses two sets of SNPs, reference SNPs and regression SNPs. The regression SNPs are SNPs that are used in a regression of χ^2 statistics from GWAS studies against the "LD scores" of those regression SNPs. The LD score of a regression SNP is a numeric score which captures the amount of genetic variation tagged by the SNP. Here, following [1] we use as regression SNPs HapMap3 SNPs, chosen for their high imputation quality, and as reference SNPs those SNPs with minor allele count greater than 5 in the 379 European samples from the 1000 Genomes Project [2]. We first compute tissue-specific scores using each of our methods for the $9,254,335$ SNPs with minor allele count greater than 5 in the 379 European samples from the 1000 Genomes Project, which we will subsequently use as our "reference SNPs" for LD score regression.

In the stratified LD score regression approach, a linear model is used to model a quantitative phenotype y_i for an individual i:

$$y_i = \sum_{j \in G} X_{ij}\beta_j + \epsilon_i.$$

bioRxiv preprint doi: https://doi.org/10.1101/069229; this version posted August 2, 2017. The copyright holder for this preprint (which was not certified by peer review) is the author/funder, who has granted bioRxiv a license to display the preprint in perpetuity. It is made available under aCC-BY-NC-ND 4.0 International license.

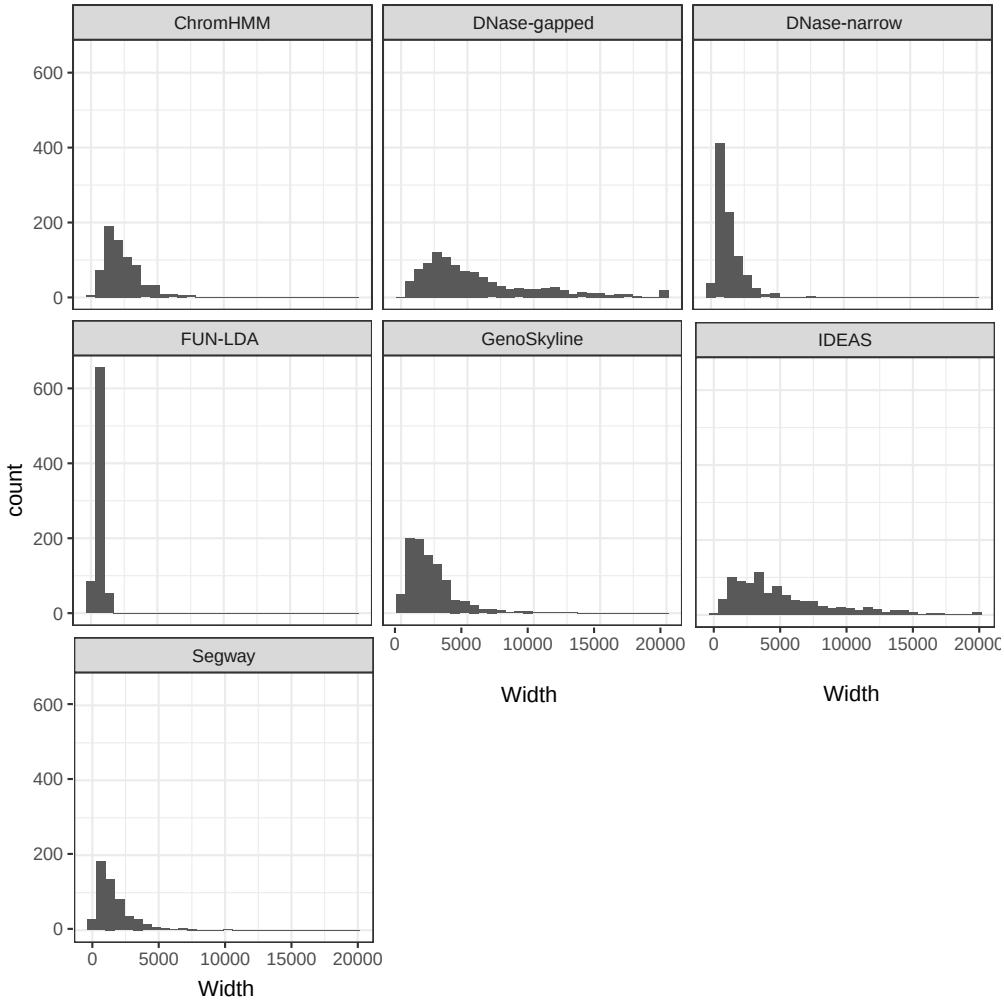

FIGURE 5. Widths of predicted functional regions (in bps) including validated functional variants from [64], [65] and the eight confirmed variants in Supplemental Table S8.

Here G is some set of SNPs, X_{ij} is the standardized genotype of individual i at SNP j, β_j is the effect size of SNP j, and ϵ_i is mean-zero noise. In this framework, $\boldsymbol{\beta}$, the vector of all the β_j, is modeled as a mean-0 random vector with independent entries, and the variance of β_j depends on the functional categories included in the model. We have a set of functional categories $C_1, \ldots, C_C$, and the variance of a SNP's effect size will depend on which functional categories it belongs to:

$$\mathrm{Var}(\beta_j) = \sum_{c: j \in C_c} \tau_c.$$

bioRxiv preprint doi: https://doi.org/10.1101/069229; this version posted August 2, 2017. The copyright holder for this preprint (which was not certified by peer review) is the author/funder, who has granted bioRxiv a license to display the preprint in perpetuity. It is made available under aCC-BY-NC-ND 4.0 International license.

Here τ_c is the per-SNP contribution to heritability of SNPs in category C_c. In [1], the authors show that under this model τ_c can be estimated through the following equation:

$$E[\chi_j^2] = N \sum_c \tau_c l(j,c) + 1.$$

Here χ_j^2 is the chi-squared statistic for SNP j from a GWAS study, N is the sample size from that study, and $l(j,c)$ is the LD score of SNP j with respect to category C_c, $l(j,c) = \sum_{k \in C_c} r_{jk}^2$. This equation therefore allows for the estimation of the τ_c via the regression of the chi-squared statistics from a GWAS study on the LD scores of the regression SNPs.

Here, we extend the stratified LD score by allowing SNPs to be assigned to a category C_c probabilistically, that is, we assume a probability p_{kc} that SNP k belongs to category C_c, and therefore that the variance of its effect size is affected by its membership in that category. This only involves minor changes to the above equations, namely, we have that

$$\mathrm{Var}(\beta_j) = \sum_{c: j \in C_c} p_{jc} \tau_c,$$

where p_{jc} is the probability that SNP j belongs to category C_c, and as above

$$E[\chi_j^2] = N \sum_c \tau_c l(j,c) + 1,$$

although now $l(j,c) = \sum_{k \in C_c} p_{kc} r_{jk}^2$, p_{kc} being the probability that SNP k belongs to category C_c. We can therefore still estimate the τ_c via the regression of the chi-squared statistics from a GWAS study on the LD scores of the regression SNPs, but in calculating these LD scores we weight the squared correlation of a SNP k with a regression SNP j by the probability that SNP k belongs to a particular category.

For each tissue and phenotype, and each of our functional scores, we fit a separate LD score regression model, including the LD score derived using the posterior probability that each regression SNP is in the functional component in that tissue, to estimate the per-SNP contribution of SNPs that belong to that component to heritability. To control for overlap of the tissue-specific functional score with other functional categories, we use the same 54 baseline categories used in [1], which represent various non-tissue-specific annotations, including histone modification measurements combined across tissues, measurements of open chromatin, and super enhancers.

bioRxiv preprint doi: https://doi.org/10.1101/069229; this version posted August 2, 2017. The copyright holder for this preprint (which was not certified by peer review) is the author/funder, who has granted bioRxiv a license to display the preprint in perpetuity. It is made available under aCC-BY-NC-ND 4.0 International license.

Summary of results for six SNPs in the literature, with evidence of regulatory function.

- rs12350739 has been shown to influence human skin color by regulating transcription of nearby *BNC2* pigmentation gene [58]. In Supplemental Figure S6 we show the predictions for Roadmap tissue E059: Foreskin Melanocyte Primary Cells skin01, the tissue we deemed closest to the one used in the functional study, melanocyte cell lines.
- rs12740374: In [59] the authors show using human-derived hepatocytes that SNP rs12740374 creates a C/EBP (CCAAT/enhancer binding protein) transcription factor binding site and alters the hepatic expression of the SORT1 gene. In Supplemental Figure S7 we show the predictions for Roadmap tissue E066: Liver, the tissue we deemed closest to the one used in the functional study, human-derived hepatocytes.
- rs356168: In [60], the authors performed allele-specific TaqMan® qRT-PCR analysis in human induced pluripotent stem cells (hIPSC)-derived neurons and show that this SNP regulates the expression of the *SNCA* gene, a gene implicated in the pathogenesis of Parkinson's disease. In Supplemental Figure S8 we show the predictions for Roadmap tissue E007: H1 Derived Neuronal Progenitor Cultured Cells, the tissue we deemed closest to the one used in the functional study, hIPSC-derived neurons.
- rs2473307: In [61], the authors showed evidence that this SNP, associated with schizophrenia, reduces expression of *CDC42* gene in a human neuronal cell line. In Supplemental Figure S9 we show the predictions for Roadmap tissue E007, H1 Derived Neuronal Progenitor Cultured Cells.
- rs227727: In [62], the authors show that this SNP, in perfect LD with the most significant GWAS variant, alters the function of an enhancer. In Supplemental Figure S10, we show the predictions for Roadmap tissue E119, HMEC Mammary Epithelial Primary Cells.
- rs144361550: In [63], the authors show that this SNP, in strong LD with a lead GWAS variant, displays allele-specific transcriptional activity in primary melanocytes. Furthermore, mass spectrometry analyses using melanoma cell line revealed that RECQL is an unequivocal allele-preferential binder of rs144361550. In Supplemental Figure S11, we show the predictions for Roadmap tissue E059: Foreskin Melanocyte Primary Cells skin01, the tissue we deemed closest to the one used in the functional study, melanocyte cell lines.

bioRxiv preprint doi: https://doi.org/10.1101/069229; this version posted August 2, 2017. The copyright holder for this preprint (which was not certified by peer review) is the author/funder, who has granted bioRxiv a license to display the preprint in perpetuity. It is made available under aCC-BY-NC-ND 4.0 International license.

Inference and parameter estimation in the variational inference procedure. It can be shown that for a single tissue the lower bound on the log likelihood can be written as

$$\begin{aligned}
L(\boldsymbol{a},\boldsymbol{w}|\boldsymbol{\alpha}) = {} & \log\Gamma(\alpha_0+\alpha_1) - \log\Gamma(\alpha_0) - \log\Gamma(\alpha_1) + (\alpha_0-1)(\Psi(a_0)-\Psi(a_0+a_1)) \\
& + (\alpha_1-1)(\Psi(a_1)-\Psi(a_0+a_1)) + \sum_{i=1}^{m} w_i(\Psi(a_1)-\Psi(a_0+a_1)) \\
& + (m-\sum_{i=1}^{m} w_i)(\Psi(a_0)-\Psi(a_0+a_1)) + \sum_{i=1}^{m}(1-w_i)\log f_0(\boldsymbol{Z}_i) + \sum_{i=1}^{m} w_i \log f_1(\boldsymbol{Z}_i) \\
& - \log\Gamma(a_0+a_1) + \log\Gamma(a_0) + \log\Gamma(a_1) - (a_0-1)(\Psi(a_0)-\Psi(a_0+a_1)) \\
& - (a_1-1)(\Psi(a_1)-\Psi(a_0+a_1)) - \sum_{i=1}^{m} w_i \log w_i - \sum_{i=1}^{m}(1-w_i)\log(1-w_i),
\end{aligned}$$

where $\Psi(x) = d\log\Gamma(x)/dx$.

Maximizing $L(\boldsymbol{a},\boldsymbol{w}|\boldsymbol{\alpha})$ with respect to $\boldsymbol{a}$ and $\boldsymbol{w}$, respectively, we get

$$w_i = \frac{f_1(\boldsymbol{Z}_i)\times\exp(\Psi(a_1))}{f_0(\boldsymbol{Z}_i)\times\exp(\Psi(a_0)) + f_1(\boldsymbol{Z}_i)\times\exp(\Psi(a_1))},$$

and

$$a_1 = \alpha_1 + \sum_{i=1}^{m} w_i \quad \text{and} \quad a_0 = \alpha_0 + \sum_{i=1}^{m}(1-w_i).$$

Given the optimal estimates of $\boldsymbol{a}$ and $\boldsymbol{w}$, we maximize the lower bound $L(\boldsymbol{a},\boldsymbol{w}|\boldsymbol{\alpha})$ with respect to the hyperparameter $\boldsymbol{\alpha}$ by using the Newton-Raphson method as in [3]. Namely, we update $\boldsymbol{\alpha}$ by iterating:

$$\boldsymbol{\alpha}^{\text{new}} = \boldsymbol{\alpha} - H(\boldsymbol{\alpha})^{-1}\nabla L(\boldsymbol{\alpha}).$$

where the gradient $\nabla L(\boldsymbol{\alpha})$ is:

$$\frac{\partial L(\boldsymbol{\alpha})}{\partial \alpha_r} = \Psi(\alpha_0+\alpha_1) - \Psi(\alpha_r) + \Psi(a_r) - \Psi(a_0+a_1) \qquad \text{for } r = 0,1,$$

and for the Hessian matrix we have:

$$H(\boldsymbol{\alpha}) = -\text{Diag}\big(\Psi'(\alpha_0),\Psi'(\alpha_1)\big) + \Psi'(\alpha_0+\alpha_1)\mathbf{1}\mathbf{1}'.$$

bioRxiv preprint doi: https://doi.org/10.1101/069229; this version posted August 2, 2017. The copyright holder for this preprint (which was not certified by peer review) is the author/funder, who has granted bioRxiv a license to display the preprint in perpetuity. It is made available under aCC-BY-NC-ND 4.0 International license.

References

[1] Finucane HK et al. (2015) Partitioning heritability by functional annotation using genome-wide association summary statistics. *Nat Genet* 47: 1228–1235.

[2] 1,000 Genomes Project Consortium (2012) An integrated map of genetic variation from 1,092 human genomes. *Nature* 491: 56–65.

[3] Blei DM, Ng AY, Jordan MI (2003) Latent Dirichlet Allocation. *Journal of Machine Learning Research* 3: 993–1022.

bioRxiv preprint doi: https://doi.org/10.1101/069229; this version posted August 2, 2017. The copyright holder for this preprint (which was not certified by peer review) is the author/funder, who has granted bioRxiv a license to display the preprint in perpetuity. It is made available under aCC-BY-NC-ND 4.0 International license.

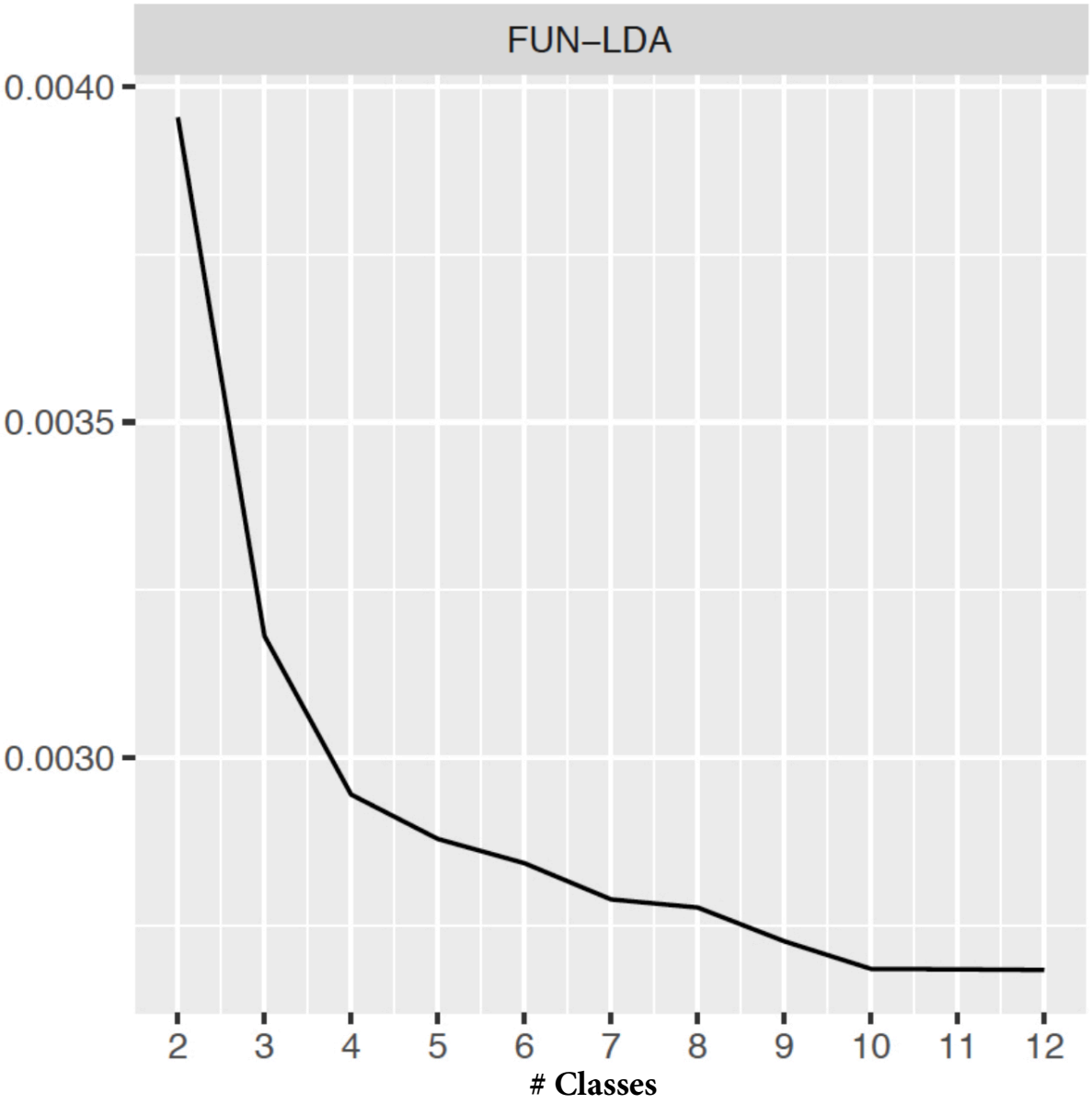

FIGURE S1. Perplexity measure of FUN-LDA models as a function of the number of classes.

bioRxiv preprint doi: https://doi.org/10.1101/069229; this version posted August 2, 2017. The copyright holder for this preprint (which was not certified by peer review) is the author/funder, who has granted bioRxiv a license to display the preprint in perpetuity. It is made available under aCC-BY-NC-ND 4.0 International license.

H3K27ac-V	H3K4me1-V	H3K4me3-V	H3K9ac-V	DNase	Size	Annotation
25.27	4.05	36.78	17.38	25.00	0.40%	ActivePromoters
2.99	2.80	1.02	0.93	4.33	1.59%	ActiveEnhancers
1.15	1.59	0.46	0.57	1.32	1.67%	WeakEnhancers
0.56	0.94	0.29	0.43	0.71	3.50%	NotFunctional
0.06	0.11	0.03	0.11	0.21	7.00%	NotFunctional
0.03	0.05	0.03	0.03	0.55	35.60%	NotFunctional
0.06	0.20	0.03	0.07	0.32	9.10%	NotFunctional
0.23	0.28	0.22	0.28	0.34	35.60%	NotFunctional
0.35	0.56	0.27	0.37	0.36	5.46%	NotFunctional

FIGURE S2. Heatmap of epigenetic features vs. class in the FUN-LDA model with nine classes across tissues and cell types in Roadmap.

bioRxiv preprint doi: https://doi.org/10.1101/069229; this version posted August 2, 2017. The copyright holder for this preprint (which was not certified by peer review) is the author/funder, who has granted bioRxiv a license to display the preprint in perpetuity. It is made available under aCC-BY-NC-ND 4.0 International license.

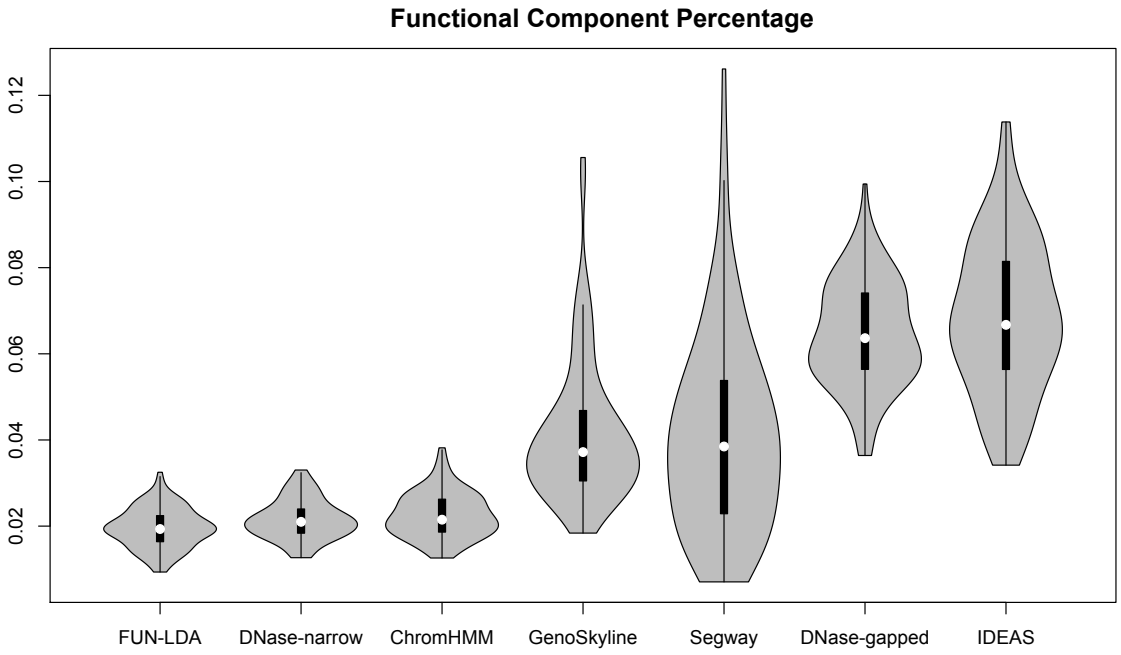

FIGURE S3. Violin plots showing the distribution of proportion of functional variants across tissues in Roadmap for each of several methods.

bioRxiv preprint doi: https://doi.org/10.1101/069229; this version posted August 2, 2017. The copyright holder for this preprint (which was not certified by peer review) is the author/funder, who has granted bioRxiv a license to display the preprint in perpetuity. It is made available under aCC-BY-NC-ND 4.0 International license.

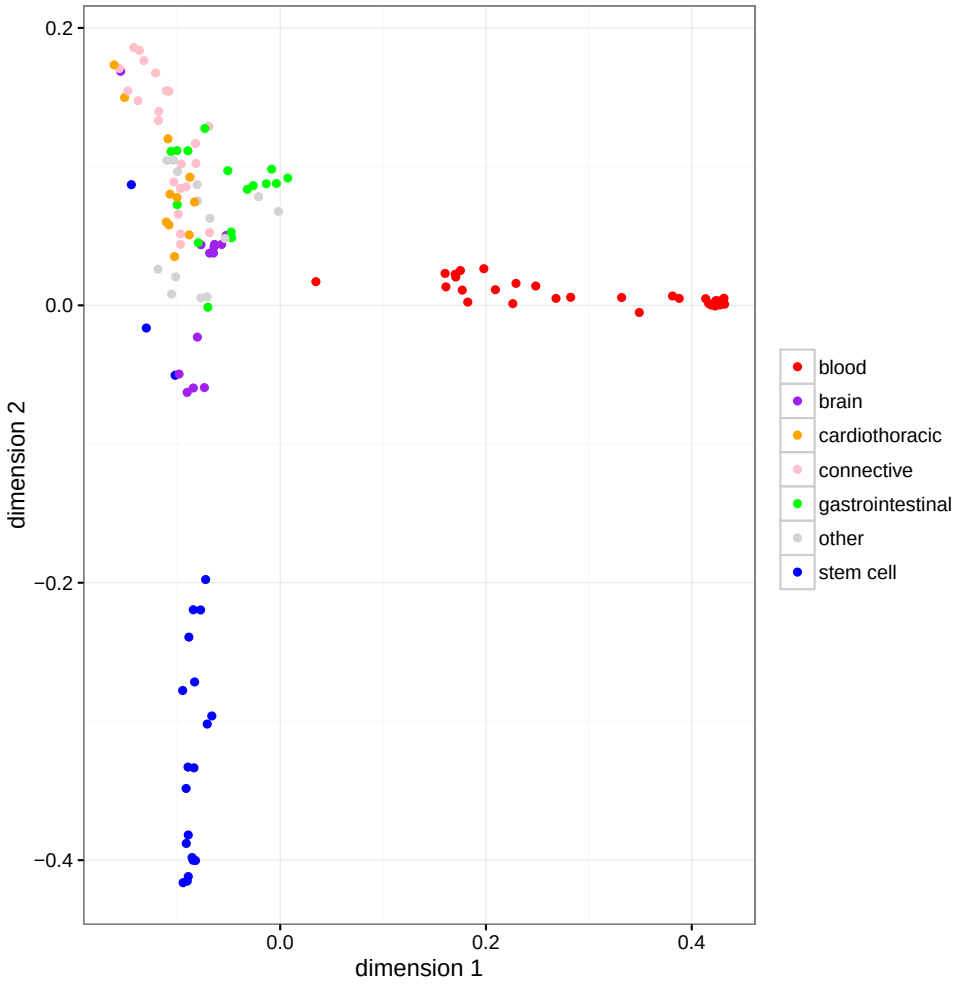

FIGURE S4. Multidimensional scaling plot of the correlations between the functional scores for the different tissues (FUN-LDA).

bioRxiv preprint doi: https://doi.org/10.1101/069229; this version posted August 2, 2017. The copyright holder for this preprint (which was not certified by peer review) is the author/funder, who has granted bioRxiv a license to display the preprint in perpetuity. It is made available under aCC-BY-NC-ND 4.0 International license.

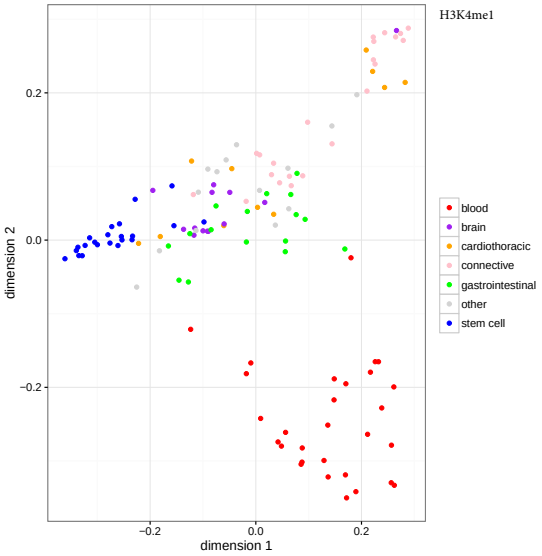

(A) H3K4me1

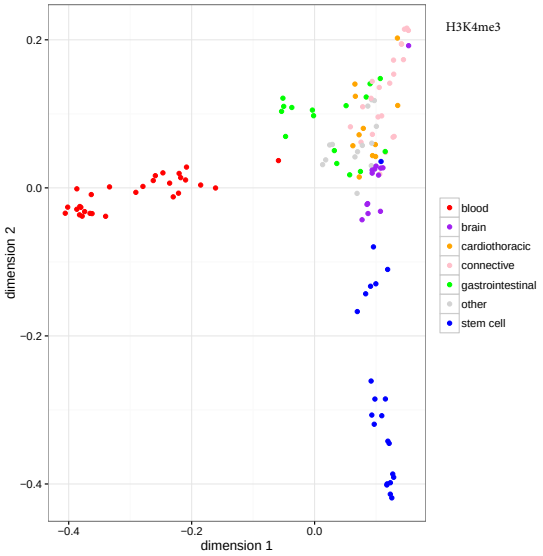

(B) H3K4me3

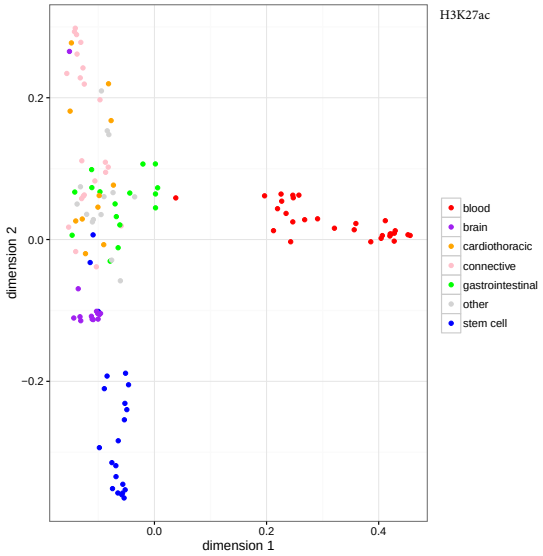

(C) H3K27ac

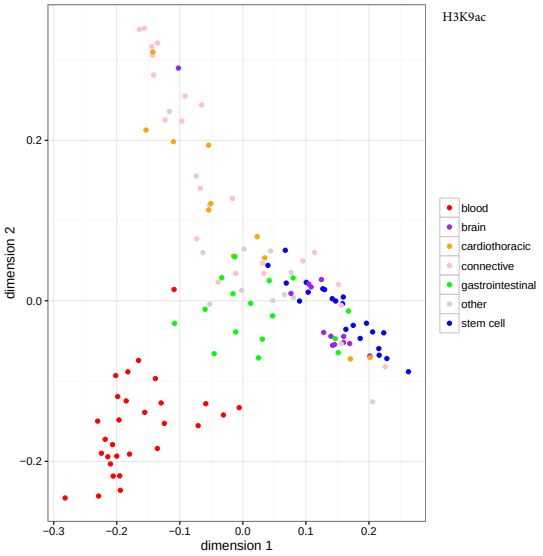

(D) H3K9ac

FIGURE S5. Multidimensional scaling plots of the correlations between the functional scores for the different tissues using individual histone marks.

bioRxiv preprint doi: https://doi.org/10.1101/069229; this version posted August 2, 2017. The copyright holder for this preprint (which was not certified by peer review) is the author/funder, who has granted bioRxiv a license to display the preprint in perpetuity. It is made available under aCC-BY-NC-ND 4.0 International license.

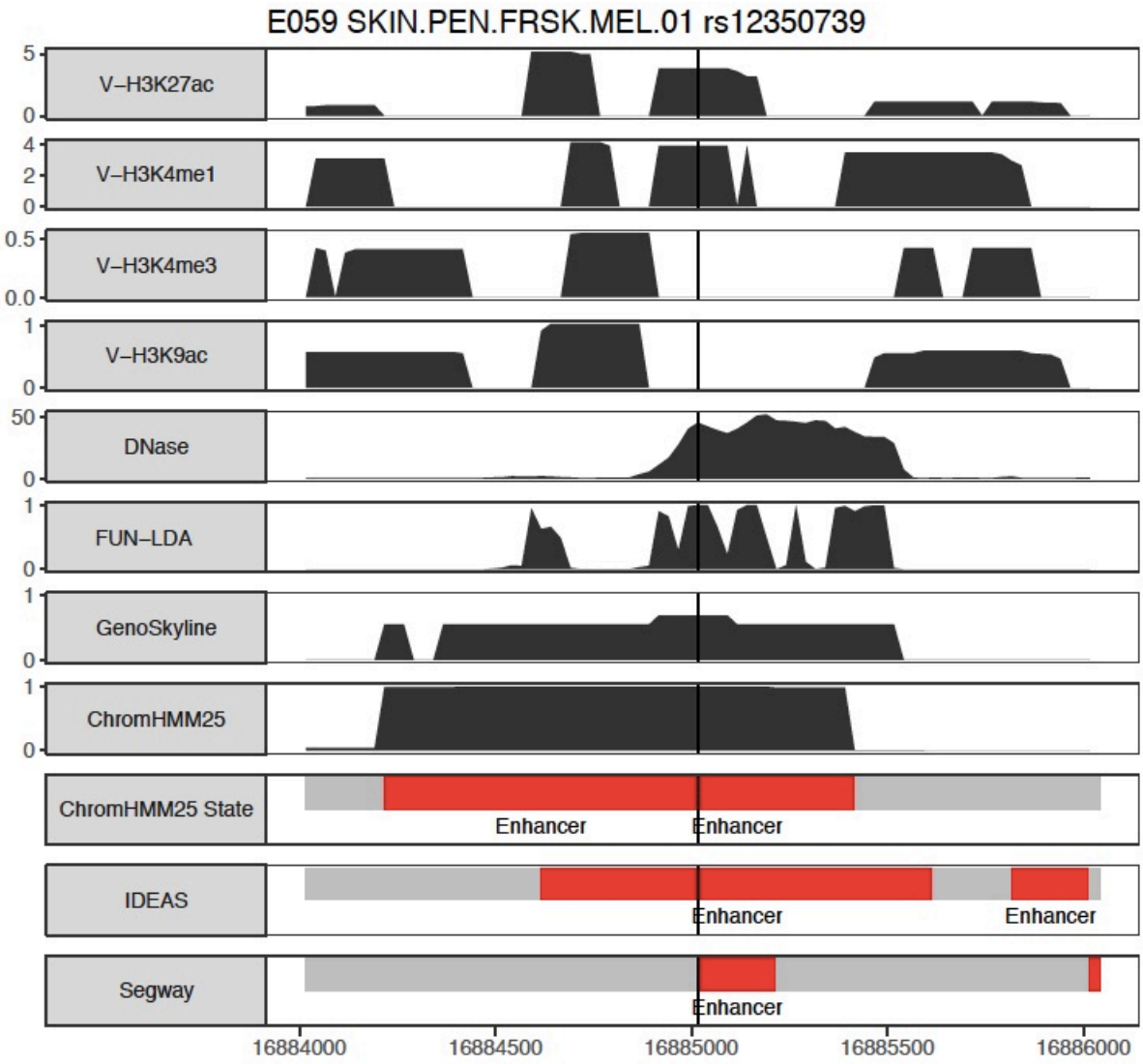

FIGURE S6. rs12350739 in Roadmap tissue E059. Valley scores for four activating histone marks and DNase, posterior probabilities from FUN-LDA, GenoSkyline, and ChromHMM (25 state model), and segmentations from ChromHMM, IDEAS and Segway are shown in 2 kb windows centered around the lead SNPs. For clarity we only highlight in the segmentations the type of states we consider functional (enhancer states in red, promoter states in blue) for the different segmentation approaches.

bioRxiv preprint doi: https://doi.org/10.1101/069229; this version posted August 2, 2017. The copyright holder for this preprint (which was not certified by peer review) is the author/funder, who has granted bioRxiv a license to display the preprint in perpetuity. It is made available under aCC-BY-NC-ND 4.0 International license.

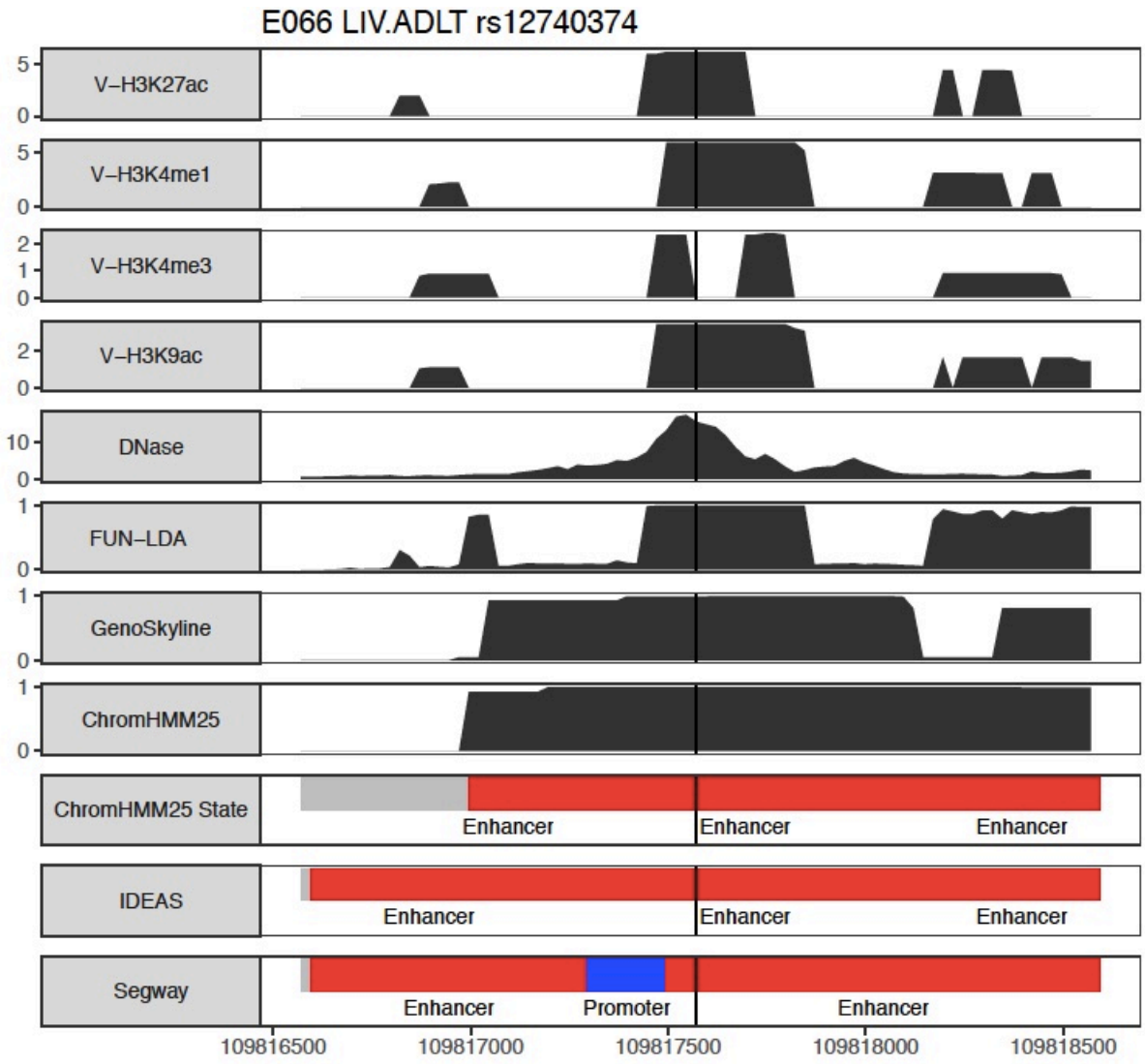

FIGURE S7. rs12740374 in Roadmap tissue E066. Valley scores for four activating histone marks and DNase, posterior probabilities from FUN-LDA, GenoSkyline, and ChromHMM (25 state model), and segmentations from ChromHMM, IDEAS and Segway are shown in 2 kb windows centered around the lead SNPs. For clarity we only highlight in the segmentations the type of states we consider functional (enhancer states in red, promoter states in blue) for the different segmentation approaches.

bioRxiv preprint doi: https://doi.org/10.1101/069229; this version posted August 2, 2017. The copyright holder for this preprint (which was not certified by peer review) is the author/funder, who has granted bioRxiv a license to display the preprint in perpetuity. It is made available under aCC-BY-NC-ND 4.0 International license.

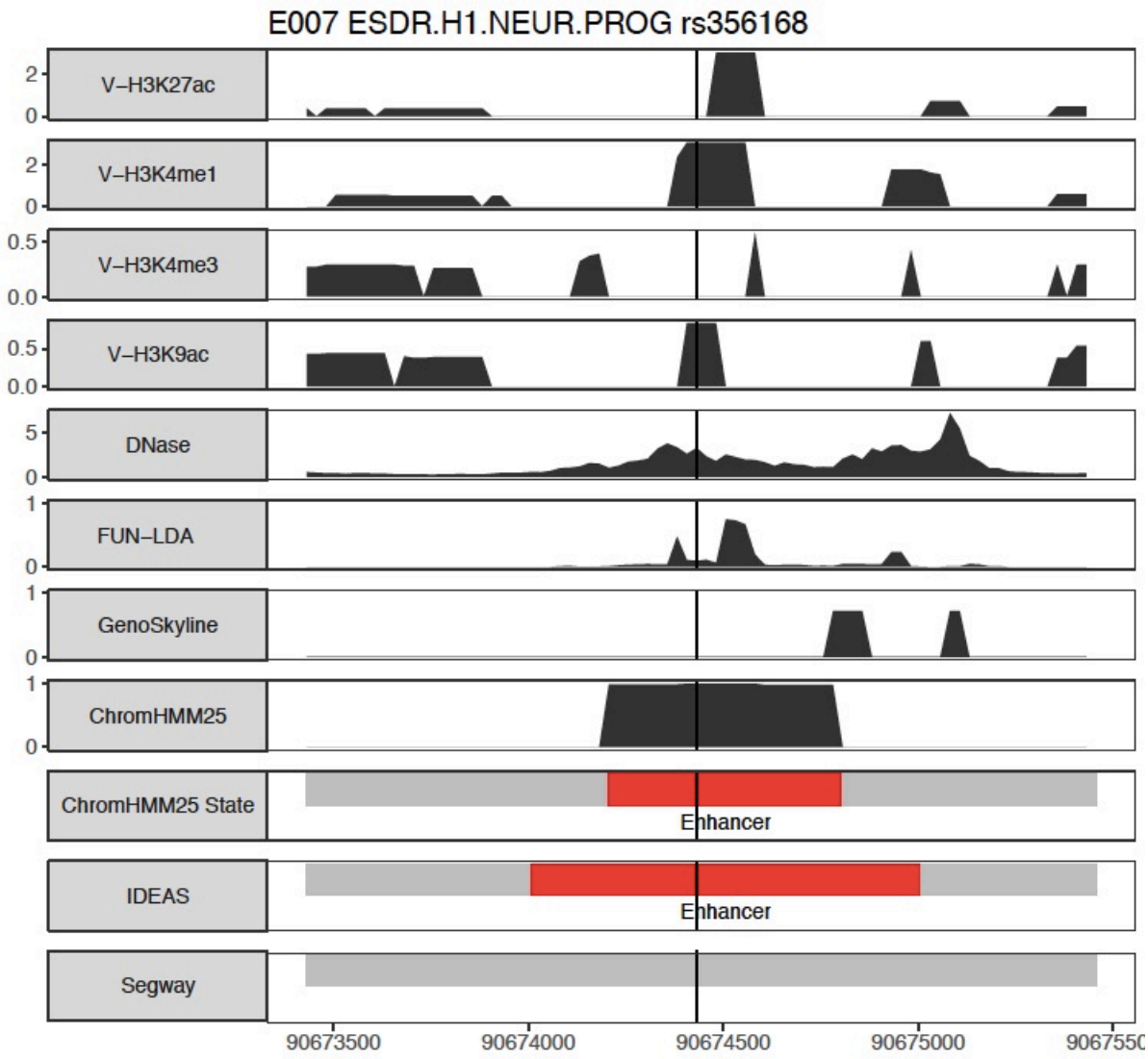

FIGURE S8. rs356168 in Roadmap tissue E007. Valley scores for four activating histone marks and DNase, posterior probabilities from FUN-LDA, GenoSkyline, and ChromHMM (25 state model), and segmentations from ChromHMM, IDEAS and Segway are shown in 2 kb windows centered around the lead SNPs. For clarity we only highlight in the segmentations the type of states we consider functional (enhancer states in red, promoter states in blue) for the different segmentation approaches.

bioRxiv preprint doi: https://doi.org/10.1101/069229; this version posted August 2, 2017. The copyright holder for this preprint (which was not certified by peer review) is the author/funder, who has granted bioRxiv a license to display the preprint in perpetuity. It is made available under aCC-BY-NC-ND 4.0 International license.

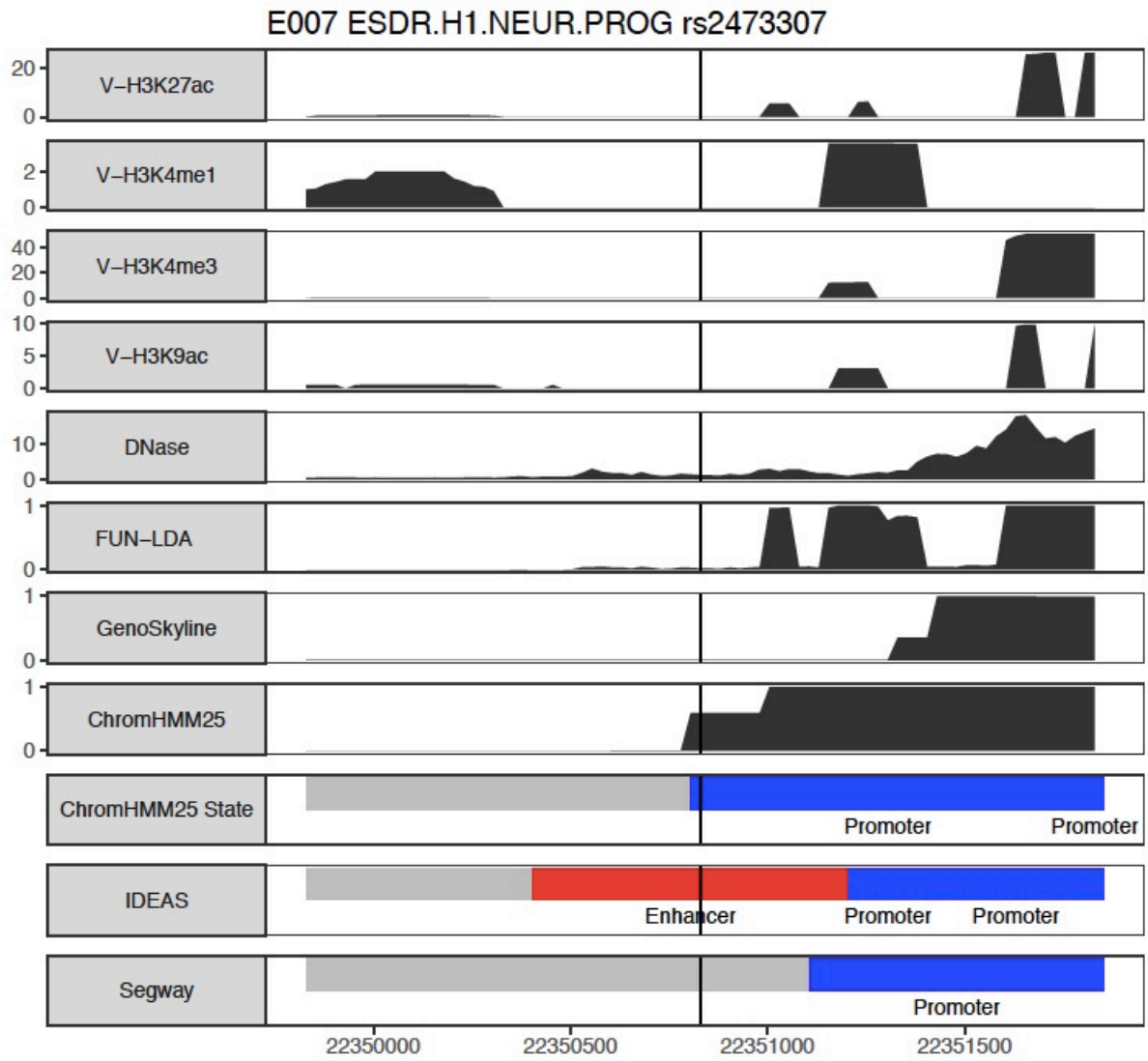

FIGURE S9. rs2473307 in Roadmap tissue E007. Valley scores for four activating histone marks and DNase, posterior probabilities from FUN-LDA, GenoSkyline, and ChromHMM (25 state model), and segmentations from ChromHMM, IDEAS and Segway are shown in 2 kb windows centered around the lead SNPs. For clarity we only highlight in the segmentations the type of states we consider functional (enhancer states in red, promoter states in blue) for the different segmentation approaches.

bioRxiv preprint doi: https://doi.org/10.1101/069229; this version posted August 2, 2017. The copyright holder for this preprint (which was not certified by peer review) is the author/funder, who has granted bioRxiv a license to display the preprint in perpetuity. It is made available under aCC-BY-NC-ND 4.0 International license.

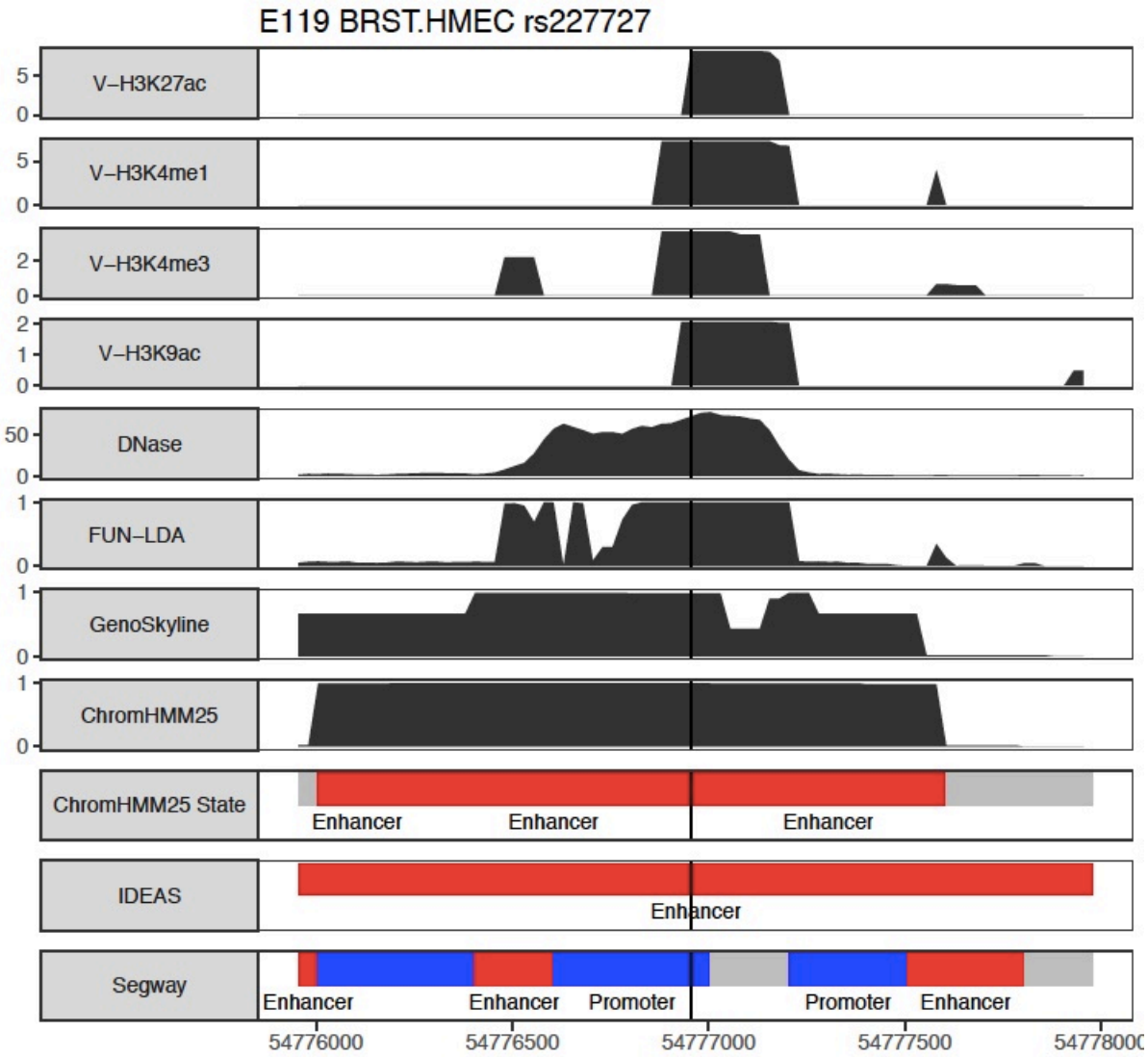

FIGURE S10. rs227727 in Roadmap tissue E119. Valley scores for four activating histone marks and DNase, posterior probabilities from FUN-LDA, GenoSkyline, and ChromHMM (25 state model), and segmentations from ChromHMM, IDEAS and Segway are shown in 2 kb windows centered around the lead SNPs. For clarity we only highlight in the segmentations the type of states we consider functional (enhancer states in red, promoter states in blue) for the different segmentation approaches.

bioRxiv preprint doi: https://doi.org/10.1101/069229; this version posted August 2, 2017. The copyright holder for this preprint (which was not certified by peer review) is the author/funder, who has granted bioRxiv a license to display the preprint in perpetuity. It is made available under aCC-BY-NC-ND 4.0 International license.

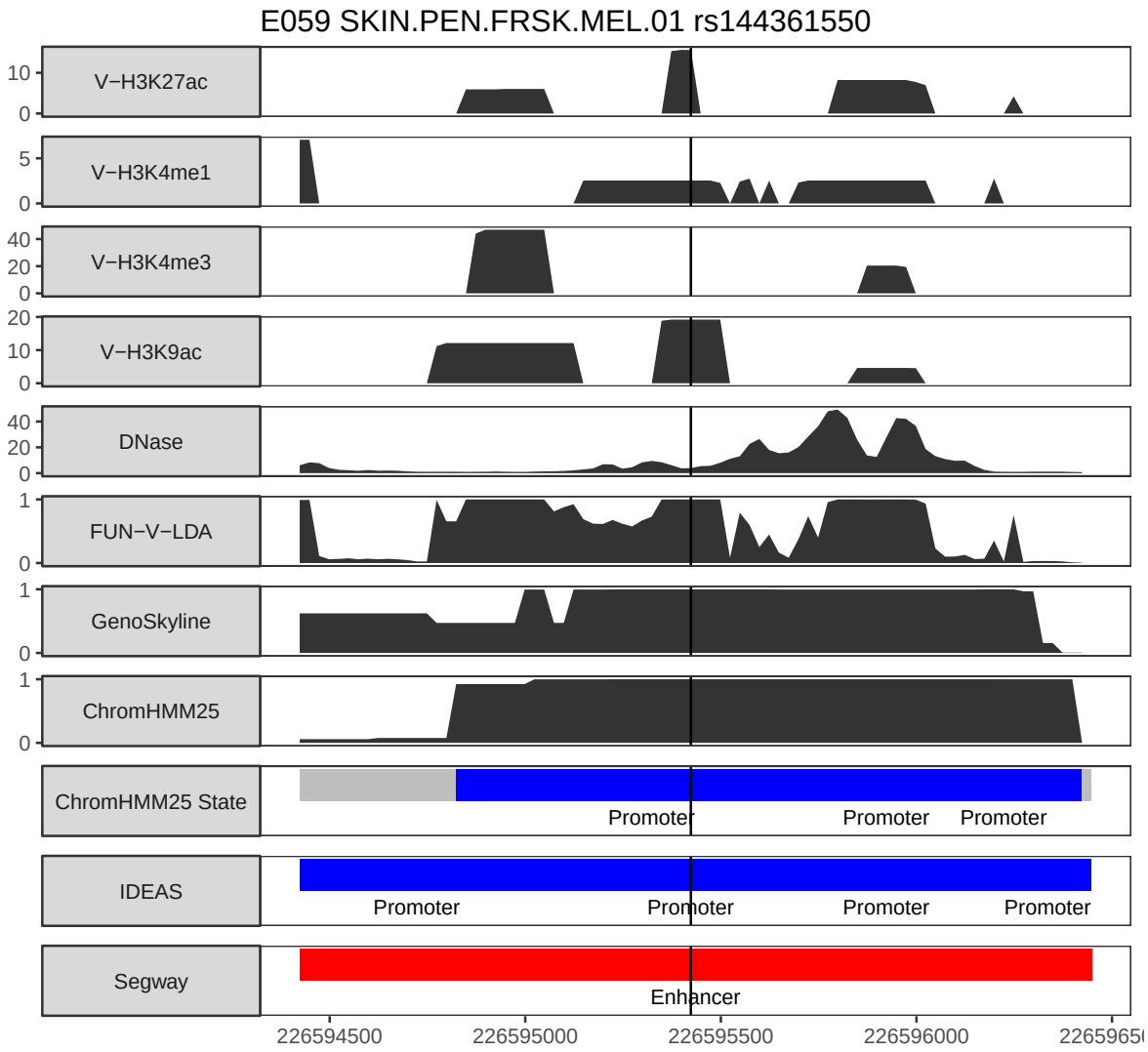

FIGURE S11. rs144361550 in Roadmap tissue E059. Valley scores for four activating histone marks and DNase, posterior probabilities from FUN-LDA, GenoSkyline, and ChromHMM (25 state model), and segmentations from ChromHMM, IDEAS and Segway are shown in 2 kb windows centered around the lead SNPs. For clarity we only highlight in the segmentations the type of states we consider functional (enhancer states in red, promoter states in blue) for the different segmentation approaches.

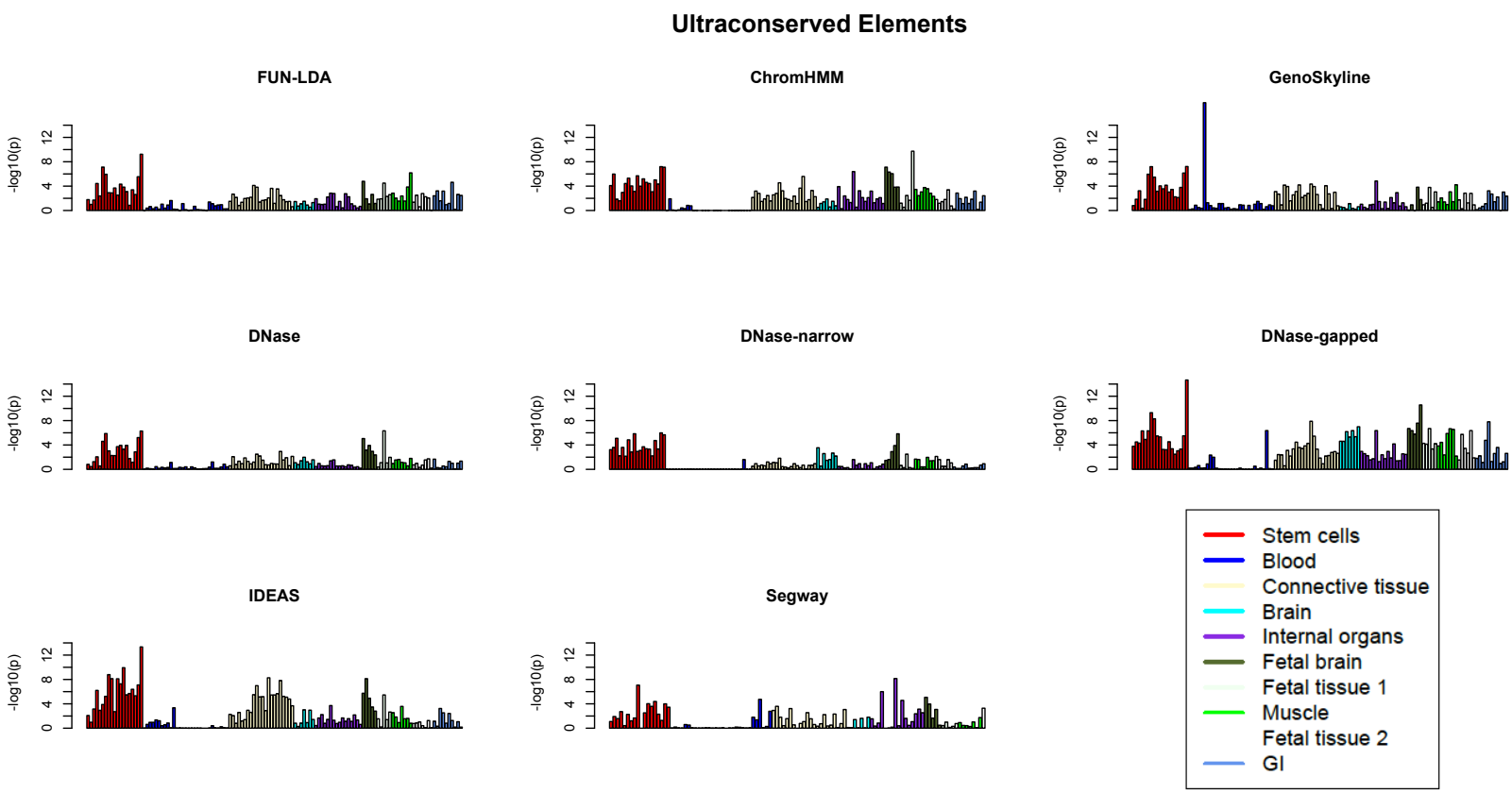

FIGURE S12. For each of several functional scores and across cell types and tissues in Roadmap, the p values from Wilcoxon rank sum test, comparing the ranks of functional scores for variants in validated enhancers in ultra conserved sequence elements vs. the ranks for the remaining variants in ultra conserved sequence elements are reported. The different tissues are grouped into several types (Supplemental Table S11).

bioRxiv preprint doi: https://doi.org/10.1101/069229; this version posted August 2, 2017. The copyright holder for this preprint (which was not certified by peer review) is the author/funder, who has granted bioRxiv a license to display the preprint in perpetuity. It is made available under aCC-BY-NC-ND 4.0 International license.

bioRxiv preprint doi: https://doi.org/10.1101/069229; this version posted August 2, 2017. The copyright holder for this preprint (which was not certified by peer review) is the author/funder, who has granted bioRxiv a license to display the preprint in perpetuity. It is made available under aCC-BY-NC-ND 4.0 International license.

Table S1. Tissues and Cell Types in Roadmap (part 1)

Epigenome.ID	Epigenome.Mnemonic	Standardized.Epigenome.name
E017	LNG.IMR90	IMR90 fetal lung fibroblasts Cell Line
E002	ESC.WA7	ES-WA7 Cells
E008	ESC.H9	H9 Cells
E001	ESC.I3	ES-I3 Cells
E015	ESC.HUES6	HUES6 Cells
E014	ESC.HUES48	HUES48 Cells
E016	ESC.HUES64	HUES64 Cells
E003	ESC.H1	H1 Cells
E024	ESC.4STAR	ES-UCSF4 Cells
E020	IPSC.20B	iPS-20b Cells
E019	IPSC.18	iPS-18 Cells
E018	IPSC.15b	iPS-15b Cells
E021	IPSC.DF.6.9	iPS DF 6.9 Cells
E022	IPSC.DF.19.11	iPS DF 19.11 Cells
E007	ESDR.H1.NEUR.PROG	H1 Derived Neuronal Progenitor Cultured Cells
E009	ESDR.H9.NEUR.PROG	H9 Derived Neuronal Progenitor Cultured Cells
E010	ESDR.H9.NEUR	H9 Derived Neuron Cultured Cells
E013	ESDR.CD56.MESO	hESC Derived CD56+ Mesoderm Cultured Cells
E012	ESDR.CD56.ECTO	hESC Derived CD56+ Ectoderm Cultured Cells
E011	ESDR.CD184.ENDO	hESC Derived CD184+ Endoderm Cultured Cells
E004	ESDR.H1.BMP4.MESO	H1 BMP4 Derived Mesendoderm Cultured Cells
E005	ESDR.H1.BMP4.TROP	H1 BMP4 Derived Trophoblast Cultured Cells
E006	ESDR.H1.MSC	H1 Derived Mesenchymal Stem Cells
E062	BLD.PER.MONUC.PC	Primary mononuclear cells from peripheral blood
E034	BLD.CD3.PPC	Primary T cells fromperipheralblood
E045	BLD.CD4.CD25I.CD127.TMEMPC	Primary T cells effector/memory enriched from peripheral blood
E033	BLD.CD3.CPC	Primary T cells from cord blood
E044	BLD.CD4.CD25.CD127M.TREGPC	Primary T regulatory cells fromperipheralblood
E043	BLD.CD4.CD25M.TPC	Primary T helper cells fromperipheralblood
E039	BLD.CD4.CD25M.CD45RA.NPC	Primary T helper naive cells fromperipheralblood
E041	BLD.CD4.CD25M.IL17M.PL.TPC	Primary T helper cells PMA-I stimulated
E042	BLD.CD4.CD25M.IL17P.PL.TPC	Primary T helper 17 cells PMA-I stimulated
E040	BLD.CD4.CD25M.CD45RO.MPC	Primary T helper memory cells from peripheral blood 1
E037	BLD.CD4.MPC	Primary T helper memory cells from peripheral blood 2
E048	BLD.CD8.MPC	Primary T CD8+ memory cells from peripheral blood
E038	BLD.CD4.NPC	Primary T helper naive cells from peripheral blood
E047	BLD.CD8.NPC	Primary T CD8+ naive cells from peripheral blood
E029	BLD.CD14.PC	Primary monocytes from peripheral blood
E031	BLD.CD19.CPC	Primary B cells from cord blood
E035	BLD.CD34.PC	Primary hematopoietic stem cells
E051	BLD.MOB.CD34.PC.M	Primary hematopoietic stem cells G-CSF-mobilized Male
E050	BLD.MOB.CD34.PC.F	Primary hematopoietic stem cells G-CSF-mobilized Female
E036	BLD.CD34.CC	Primary hematopoietic stem cells short term culture
E032	BLD.CD19.PPC	Primary B cells from peripheral blood
E046	BLD.CD56.PC	Primary Natural Killer cells from peripheral blood
E030	BLD.CD15.PC	Primary neutrophils from peripheral blood
E026	STRM.MRW.MSC	Bone Marrow Derived Cultured Mesenchymal Stem Cells
E049	STRM.CHON.MRW.DR.MSC	Mesenchymal Stem Cell Derived Chondrocyte Cultured Cells
E025	FAT.ADIP.DR.MSC	Adipose Derived Mesenchymal Stem Cell Cultured Cells
E023	FAT.MSC.DR.ADIP	Mesenchymal Stem Cell Derived Adipocyte Cultured Cells
E052	MUS.SAT	Muscle Satellite Cultured Cells
E055	SKIN.PEN.FRSK.FIB.01	Foreskin Fibroblast Primary Cells skin01
E056	SKIN.PEN.FRSK.FIB.02	Foreskin Fibroblast Primary Cells skin02
E059	SKIN.PEN.FRSK.MEL.01	Foreskin Melanocyte Primary Cells skin01
E061	SKIN.PEN.FRSK.MEL.03	Foreskin Melanocyte Primary Cells skin03
E057	SKIN.PEN.FRSK.KER.02	Foreskin Keratinocyte Primary Cells skin02
E058	SKIN.PEN.FRSK.KER.03	Foreskin Keratinocyte Primary Cells skin03
E028	BRST.HMEC.35	Breast variant Human Mammary Epithelial Cells (vHMEC)
E027	BRST.MYO	Breast Myoepithelial Primary Cells
E054	BRN.GANGEM.DR.NRSPHR	Ganglion Eminence derived primary cultured neurospheres
E053	BRN.CRTX.DR.NRSPHR	Cortex derived primary cultured neurospheres
E112	THYM	Thymus
E093	THYM.FET	Fetal Thymus

bioRxiv preprint doi: https://doi.org/10.1101/069229; this version posted August 2, 2017. The copyright holder for this preprint (which was not certified by peer review) is the author/funder, who has granted bioRxiv a license to display the preprint in perpetuity. It is made available under aCC-BY-NC-ND 4.0 International license.

Table S2. Tissues and Cell Types in Roadmap (part 2)

Epigenome.ID	Epigenome.Mnemonic	Standardized.Epigenome.name
E071	BRN.HIPP.MID	Brain Hippocampus Middle
E074	BRN.SUB.NIG	Brain Substantia Nigra
E068	BRN.ANT.CAUD	Brain Anterior Caudate
E069	BRN.CING.GYR	Brain Cingulate Gyrus
E072	BRN.INF.TMP	Brain Inferior Temporal Lobe
E067	BRN.ANG.GYR	Brain Angular Gyrus
E073	BRN.DL.PRFRNTL.CRTX	Brain_Dorsolateral_Prefrontal_Cortex
E070	BRN.GRM.MTRX	Brain Germinal Matrix
E082	BRN.FET.F	Fetal Brain Female
E081	BRN.FET.M	Fetal Brain Male
E063	FAT.ADIP.NUC	Adipose Nuclei
E100	MUS.PSOAS	Psoas Muscle
E108	MUS.SKLT.F	Skeletal Muscle Female
E107	MUS.SKLT.M	Skeletal Muscle Male
E089	MUS.TRNK.FET	Fetal Muscle Trunk
E090	MUS.LEG.FET	Fetal Muscle Leg
E083	HRT.FET	Fetal Heart
E104	HRT.ATR.R	Right Atrium
E095	HRT.VENT.L	Left Ventricle
E105	HRT.VNT.R	Right Ventricle
E065	VAS.AOR	Aorta
E078	GI.DUO.SM.MUS	Duodenum Smooth Muscle
E076	GI.CLN.SM.MUS	Colon Smooth Muscle
E103	GI.RECT.SM.MUS	Rectal Smooth Muscle
E111	GI.STMC.MUS	Stomach Smooth Muscle
E092	GI.STMC.FET	Fetal Stomach
E085	GI.S.INT.FET	Fetal Intestine Small
E084	GI.L.INT.FET	Fetal Intestine Large
E109	GI.S.INT	Small Intestine
E106	GI.CLN.SIG	Sigmoid Colon
E075	GI.CLN.MUC	Colonic Mucosa
E101	GI.RECT.MUC.29	Rectal Mucosa Donor 29
E102	GI.RECT.MUC.31	Rectal Mucosa Donor 31
E110	GI.STMC.MUC	Stomach Mucosa
E077	GI.DUO.MUC	Duodenum Mucosa
E079	GI.ESO	Esophagus
E094	GI.STMC.GAST	Gastric
E099	PLCNT.AMN	Placenta Amnion
E086	KID.FET	Fetal Kidney
E088	LNG.FET	Fetal Lung
E097	OVRY	Ovary
E087	PANC.ISLT	Pancreatic Islets
E080	ADRL.GLND.FET	Fetal Adrenal Gland
E091	PLCNT.FET	Placenta
E066	LIV.ADLT	Liver
E098	PANC	Pancreas
E096	LNG	Lung
E113	SPLN	Spleen
E114	LNG.A549.ETOH002.CNCR	A549 EtOH 0.02pct Lung Carcinoma Cell Line
E115	BLD.DND41.CNCR	Dnd41 TCell Leukemia Cell Line
E116	BLD.GM12878	GM12878 Lymphoblastoid Cells
E117	CRVX.HELAS3.CNCR	HeLa-S3 Cervical Carcinoma Cell Line
E118	LIV.HEPG2.CNCR	HepG2 Hepatocellular Carcinoma Cell Line
E119	BRST.HMEC	HMEC Mammary Epithelial Primary Cells
E120	MUS.HSMM	HSMM Skeletal Muscle Myoblasts Cells
E121	MUS.HSMMT	HSMM cell derived Skeletal Muscle Myotubes Cells
E122	VAS.HUVEC	HUVEC Umbilical Vein Endothelial Primary Cells
E123	BLD.K562.CNCR	K562 Leukemia Cells
E124	BLD.CD14.MONO	Monocytes-CD14+ RO01746 Primary Cells
E125	BRN.NHA	NH-A Astrocytes Primary Cells
E126	SKIN.NHDFAD	NHDF-Ad Adult Dermal Fibroblast Primary Cells
E127	SKIN.NHEK	NHEK-Epidermal Keratinocyte Primary Cells
E128	LNG.NHLF	NHLF Lung Fibroblast Primary Cells
E129	BONE.OSTEO	Osteoblast Primary Cells

bioRxiv preprint doi: https://doi.org/10.1101/069229; this version posted August 2, 2017. The copyright holder for this preprint (which was not certified by peer review) is the author/funder, who has granted bioRxiv a license to display the preprint in perpetuity. It is made available under aCC-BY-NC-ND 4.0 International license.

TABLE S3. Definition of the functional class for the five integrative methods considered.

Method	Functional Class Definition
FUN-LDA	States 1 and 2 (active promoters and enhancers) in Supplemental Figure S2
GenoSkyline	The functional class as defined in [23]
ChromHMM (25 state model)	1_TssA, 2_PromU, 3_PromD1, 4_PromD2, 13_EnhA1, 14_EnhA2, 15_EnhAF
Segway	Promoters and Enhancers [72]
IDEAS	4_Enh, 6_EnhG, 8_TssAFlnk, 10_TssA, 14_TssWk,17_EnhGA [21]

bioRxiv preprint doi: https://doi.org/10.1101/069229; this version posted August 2, 2017. The copyright holder for this preprint (which was not certified by peer review) is the author/funder, who has granted bioRxiv a license to display the preprint in perpetuity. It is made available under aCC-BY-NC-ND 4.0 International license.

Table S4. GTEx tissues and sample sizes.

Tissue	Sample size
Muscle - Skeletal	361
Whole Blood	338
Skin - Sun Exposed (Lower leg)	302
Adipose - Subcutaneous	298
Artery - Tibial	285
Lung	278
Thyroid	278
Cells - Transformed fibroblasts	272
Nerve - Tibial	256
Esophagus - Mucosa	241
Esophagus - Muscularis	218
Artery - Aorta	197
Skin - Not Sun Exposed (Suprapubic)	196
Heart - Left Ventricle	190
Adipose - Visceral (Omentum)	185
Breast - Mammary Tissue	183
Stomach	170
Colon - Transverse	169
Heart - Atrial Appendage	159
Testis	157
Pancreas	149
Esophagus - Gastroesophageal Junction	127
Adrenal Gland	126
Colon - Sigmoid	124
Artery - Coronary	118
Cells - EBV-transformed lymphocytes	114
Brain - Cerebellum	103
Brain - Caudate (basal ganglia)	100
Liver	97
Brain - Cortex	96
Brain - Nucleus accumbens (basal ganglia)	93
Brain - Frontal Cortex (BA9)	92
Brain - Cerebellar Hemisphere	89
Spleen	89
Pituitary	87
Prostate	87
Ovary	85
Brain - Putamen (basal ganglia)	82
Brain - Hippocampus	81
Brain - Hypothalamus	81
Vagina	79
Small Intestine - Terminal Ileum	77
Brain - Anterior cingulate cortex (BA24)	72
Uterus	70
Brain - Amygdala	62
Brain - Spinal cord (cervical c-1)	59
Brain - Substantia nigra	56
Minor Salivary Gland	51
Kidney - Cortex	26
Bladder	11
Cervix - Ectocervix	6
Fallopian Tube	6
Cervix - Endocervix	5

bioRxiv preprint doi: https://doi.org/10.1101/069229; this version posted August 2, 2017. The copyright holder for this preprint (which was not certified by peer review) is the author/funder, who has granted bioRxiv a license to display the preprint in perpetuity. It is made available under aCC-BY-NC-ND 4.0 International license.

Table S5. Results from stratified LD score regression for the different methods (part 1).

Trait	Method	Roadmap Epigenome Name	-log10(p)
AgeAtMenarche	ChromHMM	Cortex derived primary cultured neurospheres	4.31
AgeAtMenarche	DNase	hESC Derived CD56+ Ectoderm Cultured Cells	4.76
AgeAtMenarche	DNase-gapped	iPS DF 6.9 Cells	4.16
AgeAtMenarche	DNase-narrow	ES-UCSF4 Cells	7.36
AgeAtMenarche	FUN-LDA	H9 Derived Neuron Cultured Cells	6.15
AgeAtMenarche	GenoSkyline	H1 Derived Neuronal Progenitor Cultured Cells	7.96
AgeAtMenarche	IDEAS	H1 Derived Neuronal Progenitor Cultured Cells	3.47
AgeAtMenarche	Segway	H1 Derived Neuronal Progenitor Cultured Cells	9.91
Alopecia	ChromHMM	Primary T helper cells PMA-I stimulated	3.31
Alopecia	DNase	Primary T helper 17 cells PMA-I stimulated	2.10
Alopecia	DNase-gapped	Primary T helper 17 cells PMA-I stimulated	4.04
Alopecia	DNase-narrow	Primary T helper memory cells from peripheral blood 1	3.81
Alopecia	FUN-LDA	Primary T cells from cord blood	3.90
Alopecia	GenoSkyline	Primary T helper memory cells from peripheral blood 2	3.23
Alopecia	IDEAS	Primary T helper 17 cells PMA-I stimulated	4.48
Alopecia	Segway	Primary T helper 17 cells PMA-I stimulated	5.27
Alzheimers	ChromHMM	Primary hematopoietic stem cells	1.86
Alzheimers	DNase	Monocytes-CD14+ RO01746 Primary Cells	2.05
Alzheimers	DNase-gapped	Primary hematopoietic stem cells G-CSF-mobilized Male	3.96
Alzheimers	DNase-narrow	Primary hematopoietic stem cells G-CSF-mobilized Male	3.59
Alzheimers	FUN-LDA	Primary hematopoietic stem cells G-CSF-mobilized Male	3.78
Alzheimers	GenoSkyline	Monocytes-CD14+ RO01746 Primary Cells	2.91
Alzheimers	IDEAS	Primary hematopoietic stem cells G-CSF-mobilized Male	4.06
Alzheimers	Segway	Primary hematopoietic stem cells G-CSF-mobilized Male	3.79
Autism	ChromHMM	Fetal Brain Female	1.19
Autism	DNase	Primary monocytes from peripheral blood	1.64
Autism	DNase-gapped	Primary monocytes from peripheral blood	2.16
Autism	DNase-narrow	Monocytes-CD14+ RO01746 Primary Cells	1.94
Autism	FUN-LDA	Primary monocytes from peripheral blood	2.41
Autism	GenoSkyline	Brain Dorsolateral Prefrontal Cortex	1.26
Autism	IDEAS	Liver	2.54
Autism	Segway	Monocytes-CD14+ RO01746 Primary Cells	2.34
BipolarDisorder	ChromHMM	Primary monocytes from peripheral blood	2.27
BipolarDisorder	DNase	Monocytes-CD14+ RO01746 Primary Cells	2.23
BipolarDisorder	DNase-gapped	Monocytes-CD14+ RO01746 Primary Cells	3.48
BipolarDisorder	DNase-narrow	Monocytes-CD14+ RO01746 Primary Cells	2.48
BipolarDisorder	FUN-LDA	Fetal Brain Female	3.20
BipolarDisorder	GenoSkyline	Psoas Muscle	3.73
BipolarDisorder	IDEAS	Fetal Brain Male	3.30
BipolarDisorder	Segway	Brain Dorsolateral Prefrontal Cortex	3.70
BMI	ChromHMM	Fetal Brain Female	2.94
BMI	DNase	ES-UCSF4 Cells	1.12
BMI	DNase-gapped	ES-UCSF4 Cells	2.58
BMI	DNase-narrow	ES-UCSF4 Cells	4.29
BMI	FUN-LDA	Brain Germinal Matrix	4.79
BMI	GenoSkyline	Brain Dorsolateral Prefrontal Cortex	6.47
BMI	IDEAS	Brain Angular Gyrus	4.44
BMI	Segway	iPS DF 19.11 Cells	4.49
CoronaryArteryDisease	ChromHMM	Liver	3.38
CoronaryArteryDisease	DNase	Liver	2.62
CoronaryArteryDisease	DNase-gapped	Liver	4.67
CoronaryArteryDisease	DNase-narrow	Lung	3.51
CoronaryArteryDisease	FUN-LDA	Liver	4.61
CoronaryArteryDisease	GenoSkyline	Lung	4.25
CoronaryArteryDisease	IDEAS	Adipose Nuclei	3.65
CoronaryArteryDisease	Segway	Small Intestine	5.70

bioRxiv preprint doi: https://doi.org/10.1101/069229; this version posted August 2, 2017. The copyright holder for this preprint (which was not certified by peer review) is the author/funder, who has granted bioRxiv a license to display the preprint in perpetuity. It is made available under aCC-BY-NC-ND 4.0 International license.

Table S6. Results from stratified LD score regression for the different methods (part 2).

Trait	Method	Roadmap Epigenome Name	-log10(p)
CrohnsDisease	ChromHMM	Primary T helper 17 cells PMA-I stimulated	6.39
CrohnsDisease	DNase	Primary T helper cells PMA-I stimulated	3.84
CrohnsDisease	DNase-gapped	Primary B cells from peripheral blood	6.89
CrohnsDisease	DNase-narrow	Primary T helper 17 cells PMA-I stimulated	6.90
CrohnsDisease	FUN-LDA	Primary B cells from cord blood	6.25
CrohnsDisease	GenoSkyline	Primary Natural Killer cells from peripheral blood	4.95
CrohnsDisease	IDEAS	Primary T helper memory cells from peripheral blood 1	7.60
CrohnsDisease	Segway	Primary T helper 17 cells PMA-I stimulated	7.53
EducationalAttainment	ChromHMM	Fetal Brain Female	4.74
EducationalAttainment	DNase	Fetal Brain Female	3.05
EducationalAttainment	DNase-gapped	Cortex derived primary cultured neurospheres	4.27
EducationalAttainment	DNase-narrow	Fetal Brain Female	3.07
EducationalAttainment	FUN-LDA	Fetal Brain Female	5.84
EducationalAttainment	GenoSkyline	Brain Dorsolateral Prefrontal Cortex	3.61
EducationalAttainment	IDEAS	Fetal Brain Female	7.32
EducationalAttainment	Segway	Fetal Brain Male	5.55
Epilepsy	ChromHMM	Brain Angular Gyrus	2.91
Epilepsy	DNase	Dnd41 TCell Leukemia Cell Line	0.99
Epilepsy	DNase-gapped	Brain Hippocampus Middle	2.36
Epilepsy	DNase-narrow	Fetal Thymus	1.85
Epilepsy	FUN-LDA	Brain Anterior Caudate	4.11
Epilepsy	GenoSkyline	Brain Inferior Temporal Lobe	3.35
Epilepsy	IDEAS	Brain Angular Gyrus	4.40
Epilepsy	Segway	Brain Angular Gyrus	4.51
EverSmoked	ChromHMM	Primary T cells effector/memory enriched from peripheral blood	2.15
EverSmoked	DNase	Brain Inferior Temporal Lobe	0.61
EverSmoked	DNase-gapped	Brain Inferior Temporal Lobe	1.31
EverSmoked	DNase-narrow	Primary hematopoietic stem cells	0.78
EverSmoked	FUN-LDA	Brain Inferior Temporal Lobe	2.68
EverSmoked	GenoSkyline	Brain Inferior Temporal Lobe	2.94
EverSmoked	IDEAS	Brain Angular Gyrus	3.66
EverSmoked	Segway	Brain Inferior Temporal Lobe	4.16
FastingGlucose	ChromHMM	Pancreatic Islets	1.44
FastingGlucose	DNase	Fetal Intestine Small	1.03
FastingGlucose	DNase-gapped	Pancreatic Islets	2.03
FastingGlucose	DNase-narrow	iPS-15b Cells	1.60
FastingGlucose	FUN-LDA	Pancreatic Islets	1.45
FastingGlucose	GenoSkyline	H9 Cells	2.29
FastingGlucose	IDEAS	Pancreatic Islets	3.65
FastingGlucose	Segway	Pancreatic Islets	3.85
HDL	ChromHMM	Primary monocytes from peripheral blood	2.72
HDL	DNase	Liver	3.94
HDL	DNase-gapped	Adipose Nuclei	5.15
HDL	DNase-narrow	Adipose Nuclei	4.37
HDL	FUN-LDA	Liver	4.73
HDL	GenoSkyline	Liver	3.67
HDL	IDEAS	Adipose Nuclei	5.63
HDL	Segway	Liver	4.28
Height	ChromHMM	Mesenchymal Stem Cell Derived Chondrocyte Cultured Cells	5.55
Height	DNase	Mesenchymal Stem Cell Derived Chondrocyte Cultured Cells	4.45
Height	DNase-gapped	Mesenchymal Stem Cell Derived Chondrocyte Cultured Cells	9.99
Height	DNase-narrow	Mesenchymal Stem Cell Derived Chondrocyte Cultured Cells	10.81
Height	FUN-LDA	Mesenchymal Stem Cell Derived Chondrocyte Cultured Cells	12.28
Height	GenoSkyline	Mesenchymal Stem Cell Derived Chondrocyte Cultured Cells	11.31
Height	IDEAS	Mesenchymal Stem Cell Derived Chondrocyte Cultured Cells	14.59
Height	Segway	Mesenchymal Stem Cell Derived Chondrocyte Cultured Cells	13.40

bioRxiv preprint doi: https://doi.org/10.1101/069229; this version posted August 2, 2017. The copyright holder for this preprint (which was not certified by peer review) is the author/funder, who has granted bioRxiv a license to display the preprint in perpetuity. It is made available under aCC-BY-NC-ND 4.0 International license.

TABLE S7. Results from stratified LD score regression for the different methods (part 3).

Trait	Method	Roadmap Epigenome Name	-log10(p)
IGAN	ChromHMM	Dnd41 TCell Leukemia Cell Line	2.35
IGAN	DNase	Monocytes-CD14+ RO01746 Primary Cells	1.59
IGAN	DNase-gapped	Primary T cells from peripheral blood	3.86
IGAN	DNase-narrow	Primary T helper memory cells from peripheral blood 2	4.13
IGAN	FUN-LDA	Primary Natural Killer cells from peripheral blood	3.28
IGAN	GenoSkyline	Primary mononuclear cells from peripheral blood	3.64
IGAN	IDEAS	Primary T cells from peripheral blood	3.65
IGAN	Segway	Primary Natural Killer cells from peripheral blood	3.23
LDL	ChromHMM	Liver	3.25
LDL	DNase	Liver	1.61
LDL	DNase-gapped	Liver	3.68
LDL	DNase-narrow	Fetal Adrenal Gland	2.64
LDL	FUN-LDA	Liver	4.08
LDL	GenoSkyline	Liver	4.37
LDL	IDEAS	Liver	5.06
LDL	Segway	Liver	4.29
RheumatoidArthritis	ChromHMM	GM12878 Lymphoblastoid Cells	8.25
RheumatoidArthritis	DNase	Primary T helper cells PMA-I stimulated	4.27
RheumatoidArthritis	DNase-gapped	Primary T helper cells PMA-I stimulated	7.60
RheumatoidArthritis	DNase-narrow	Primary T helper cells PMA-I stimulated	7.51
RheumatoidArthritis	FUN-LDA	GM12878 Lymphoblastoid Cells	6.93
RheumatoidArthritis	GenoSkyline	Primary B cells from peripheral blood	5.83
RheumatoidArthritis	IDEAS	GM12878 Lymphoblastoid Cells	8.84
RheumatoidArthritis	Segway	Primary T helper 17 cells PMA-I stimulated	7.93
Schizophrenia	ChromHMM	Fetal Brain Female	11.88
Schizophrenia	DNase	Brain Germinal Matrix	6.64
Schizophrenia	DNase-gapped	Fetal Brain Female	9.01
Schizophrenia	DNase-narrow	Fetal Brain Female	9.12
Schizophrenia	FUN-LDA	Fetal Brain Female	14.70
Schizophrenia	GenoSkyline	Brain Dorsolateral Prefrontal Cortex	8.95
Schizophrenia	IDEAS	Fetal Brain Male	Inf
Schizophrenia	Segway	Fetal Brain Male	Inf
Triglycerides	ChromHMM	Liver	3.49
Triglycerides	DNase	Liver	4.05
Triglycerides	DNase-gapped	Liver	4.89
Triglycerides	DNase-narrow	Liver	4.06
Triglycerides	FUN-LDA	Liver	4.11
Triglycerides	GenoSkyline	Liver	3.63
Triglycerides	IDEAS	Liver	4.30
Triglycerides	Segway	Liver	3.86
Type2Diabetes	ChromHMM	Fetal Kidney	1.79
Type2Diabetes	DNase	Fetal Intestine Small	1.27
Type2Diabetes	DNase-gapped	Pancreatic Islets	3.67
Type2Diabetes	DNase-narrow	HepG2 Hepatocellular Carcinoma Cell Line	2.91
Type2Diabetes	FUN-LDA	Pancreatic Islets	4.21
Type2Diabetes	GenoSkyline	Adipose Nuclei	2.18
Type2Diabetes	IDEAS	Fetal Intestine Small	3.03
Type2Diabetes	Segway	Pancreatic Islets	3.27
UlcerativeColitis	ChromHMM	Primary T helper 17 cells PMA-I stimulated	4.26
UlcerativeColitis	DNase	Primary T helper cells PMA-I stimulated	2.06
UlcerativeColitis	DNase-gapped	Primary T helper 17 cells PMA-I stimulated	3.95
UlcerativeColitis	DNase-narrow	Primary T helper 17 cells PMA-I stimulated	4.84
UlcerativeColitis	FUN-LDA	Primary T helper 17 cells PMA-I stimulated	4.45
UlcerativeColitis	GenoSkyline	Rectal Mucosa Donor 29	3.54
UlcerativeColitis	IDEAS	Primary T helper 17 cells PMA-I stimulated	4.97
UlcerativeColitis	Segway	Primary T helper 17 cells PMA-I stimulated	5.77

bioRxiv preprint doi: https://doi.org/10.1101/069229; this version posted August 2, 2017. The copyright holder for this preprint (which was not certified by peer review) is the author/funder, who has granted bioRxiv a license to display the preprint in perpetuity. It is made available under aCC-BY-NC-ND 4.0 International license.

TABLE S8. For eight SNPs selected from literature, the tissue or cell type in the original study and the closest tissue in Roadmap that we selected are given.

SNP	Tissue in Functional Study	Selected Roadmap Tissue
rs6801957	murine heart tissue	E104 - Right Atrium
rs12821256	cultured human keratinocytes	E127 - NHEK-Epidermal Keratinocyte Primary Cells
rs12350739	skin epidermal samples/melanocyte cell lines	E059 - Foreskin Melanocyte Primary Cells skin01
rs12740374	primary hepatocytes	E066 - Liver
rs356168	hIPSC-derived neurons	E007 - H1 Derived Neuronal Progenitor Cultured Cells
rs2473307	human neuronal cell line	E007 - H1 Derived Neuronal Progenitor Cultured Cells
rs227727	human embryonic oral epithelial cells	E119 - HMEC Mammary Epithelial Primary Cells
rs144361550	primary melanocytes	E059 - Foreskin Melanocyte Primary Cells skin01

TABLE S9. AUC for various integrative methods vs. individual epigenetic annotations using MPRA validated variants.

Method	Type	emVars	Regulatory motifs	Regulatory motifs
		E116	E118	E123
FUN-LDA		0.709	0.694	0.646
GenoSkyline		0.674	0.630	0.619
ChromHMM	Integrative	0.668	0.608	0.634
Segway		0.624	0.618	0.585
IDEAS		0.621	0.546	0.615
DNase		0.722	0.719	0.654
DNase-narrow		0.629	0.561	0.524
DNase-gapped		0.653	0.550	0.565
H3K27ac	Single annotation	0.677	0.556	0.597
H3K4me1		0.664	0.545	0.578
H3K4me3		0.692	0.535	0.602
H3K9ac		0.670	0.549	0.615

TABLE S10. AUC for the segmentation methods ChromHMM, Segway and IDEAS state combinations with maximum AUC using the MPRA validated variants. Note that the selection of the best state combination is based on combining the variants from all three MPRA datasets in Section 2.4.

Method	TypeState	States in 'functional' group	emVars	Reg. motifs	Reg. motifs
			E116	E118	E123
FUN-LDA	Selected	1_ActiveEnhancers, 2_ActivePromoters	0.709	0.694	0.646
ChromHMM	Best	1_TssA, 2_PromU, 9_TxReg, 13_EnhA1 14_EnhA2, 16_EnhW1, 22_PromP	0.670	0.619	0.661
	Selected	1_TssA, 2_PromU, 3_PromD1, 4_PromD2 13_EnhA1, 14_EnhA2, 15_EnhAF	0.668	0.608	0.634
Segway	Best	Bivalent, RegPermissive, Enhancer, Promoter	0.650	0.591	0.630
	Selected	Enhancer, Promoter	0.624	0.618	0.585
IDEAS	Best	4_Enh, 8_TssAFlnk, 6_EnhG, 10_TssA 19_Enh/ReprPC,11_EnhBiv,15_TssBiv,14_TssWk,17_EnhGA	0.635	0.544	0.614
	Selected	4_Enh, 6_EnhG, 8_TssAFlnk, 10_TssA, 14_TssWk,17_EnhGA	0.621	0.546	0.615

bioRxiv preprint doi: https://doi.org/10.1101/069229; this version posted August 2, 2017. The copyright holder for this preprint (which was not certified by peer review) is the author/funder, who has granted bioRxiv a license to display the preprint in perpetuity. It is made available under aCC-BY-NC-ND 4.0 International license.

TABLE S11. Grouping of Roadmap tissues into 10 tissue types.

Epigenome.ID	Type	Epigenome.ID	Type
E022	Stem cell	E117	Connective tissue
E007	Stem cell	E028	Connective tissue
E004	Stem cell	E057	Connective tissue
E002	Stem cell	E058	Connective tissue
E021	Stem cell	E119	Connective tissue
E009	Stem cell	E127	Connective tissue
E010	Stem cell	E071	Brain
E001	Stem cell	E074	Brain
E015	Stem cell	E073	Brain
E018	Stem cell	E068	Brain
E016	Stem cell	E067	Brain
E020	Stem cell	E069	Brain
E014	Stem cell	E072	Brain
E019	Stem cell	E027	Internal organs
E024	Stem cell	E059	Internal organs
E008	Stem cell	E061	Internal organs
E003	Stem cell	E065	Internal organs
E012	Stem cell	E097	Internal organs
E011	Stem cell	E086	Internal organs
E115	Blood	E087	Internal organs
E123	Blood	E100	Internal organs
E030	Blood	E105	Internal organs
E029	Blood	E104	Internal organs
E124	Blood	E095	Internal organs
E035	Blood	E096	Internal organs
E036	Blood	E113	Internal organs
E051	Blood	E079	Internal organs
E050	Blood	E094	Internal organs
E034	Blood	E098	Internal organs
E046	Blood	E081	Fetal brain
E041	Blood	E070	Fetal brain
E047	Blood	E082	Fetal brain
E048	Blood	E054	Fetal brain
E038	Blood	E053	Fetal brain
E045	Blood	E005	Fetal tissue 1
E044	Blood	E099	Fetal tissue 1
E043	Blood	E013	Fetal tissue 1
E039	Blood	E006	Fetal tissue 1
E042	Blood	E083	Fetal tissue 1
E040	Blood	E108	Muscle
E037	Blood	E107	Muscle
E112	Blood	E063	Muscle
E093	Blood	E078	Muscle
E062	Blood	E103	Muscle
E033	Blood	E076	Muscle
E116	Blood	E111	Muscle
E031	Blood	E091	Fetal tissue 2
E032	Blood	E092	Fetal tissue 2
E122	Connective tissue	E089	Fetal tissue 2
E120	Connective tissue	E090	Fetal tissue 2
E121	Connective tissue	E088	Fetal tissue 2
E025	Connective tissue	E080	Fetal tissue 2
E023	Connective tissue	E066	GI
E049	Connective tissue	E110	GI
E026	Connective tissue	E109	GI
E129	Connective tissue	E106	GI
E126	Connective tissue	E075	GI
E052	Connective tissue	E077	GI
E125	Connective tissue	E101	GI
E055	Connective tissue	E102	GI
E056	Connective tissue	E118	GI
E017	Connective tissue	E085	GI
E128	Connective tissue	E084	GI
E114	Connective tissue		